DEVELOPMENT OF NON-UNIFORM RADIATION SOLUTION METHODS FOR
ATMOSPHERIC RE-ENTRY USING DETAILED THERMAL MODELING

THESIS

Jeffrey R. Komives, Captain, USAF

AFIT/GAE/ENY/09-M13

DEPARTMENT OF THE AIR FORCE
AIR UNIVERSITY

AIR FORCE INSTITUTE OF TECHNOLOGY

Wright Patterson Air Force Base, Ohio

AFIT/GAE/ENY/09-M13

DEVELOPMENT OF NON-UNIFORM RADIATION SOLUTION METHODS
FOR ATMOSPHERIC RE-ENTRY USING DETAILED THERMAL MODELING

THESIS

Presented to the Faculty of the

Department of Aeronautics and Astronautics

Graduate School of Engineering and Management

Air Force Institute of Technology

Air University

Air Education and Training Command

in Partial Fulfillment of the Requirements for the

Degree of Master of Science in Aeronautical Engineering

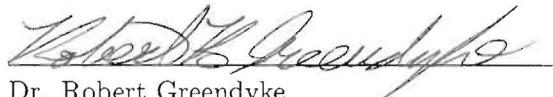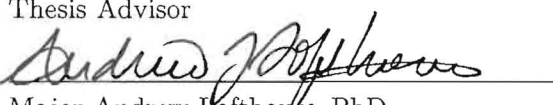Jeffrey R. Komives

Captain, USAF

March, 2009

DEVELOPMENT OF NON-UNIFORM RADIATION SOLUTION METHODS FOR ATMOSPHERIC RE-ENTRY USING DETAILED THERMAL MODELING

Jeffrey R. Komives

Captain, USAF

Approved:

Dr. Robert Greendyke   12 May 2009
Thesis Advisor   Date

Major Andrew Lofthouse PhD   12 Mar 2009
Committee Member   Date

Major Richard Huffman PhD   12 Mar 09
Committee Member   Date

AFIT/GAE/ENY/09-M13

Abstract

The line-by-line accurate spectral radiation solver SPRADIAN was integrated with the multi-temperature hypersonic flow-solver NH7Air for the purpose of predicting the radiation incident on the surface of a hypersonic re-entry vehicle. Atomic and molecular radiation mechanisms are considered for chemical species present in an Earth atmosphere re-entry. A new numerical method of radiation propagation is presented that is capable of accurately predicting the radiation propagation through a non-uniform radiation field. This method also introduces a unique treatment of the internal energy of each chemical species, independently tracking the vibrational temperatures of all molecular species.

The new radiation propagation method is validated against the industry standard tangent-slab method for a uniform radiating slab. Results are also presented for the 1636 second trajectory point of the NASA FIRE-II experiment. For the FIRE-II case, the results of the new method is compared to the results of the tangent-slab analysis, and with the values measured in the experiment.

Acknowledgements

Jeffrey R. Komives

Table of Contents

List of Figures

List of Tables

List of Abbreviations

DEVELOPMENT OF NON-UNIFORM RADIATION SOLUTION METHODS FOR ATMOSPHERIC RE-ENTRY USING DETAILED THERMAL MODELING

1.   INTRODUCTION

The task of providing rapid, responsive access to space provides numerous technical challenges to the Air Force in the 21st century. By having responsive, low-cost access to space, theater commanders and combatant commanders will be able to use space as a warfighting domain, not just in a strategic sense but in an operational or tactical sense. Vehicles providing this capability need to be light-weight and rapidly serviceable. The original intention of the STS program was to provide just such a vehicle. Due to a myriad of reliability, maintainability, and safety issues, the Space Shuttle has been unable to provide truly rapid, responsive access to space

To address issues in the operational life of the Shuttle, vehicle planners and designers are re-visiting carbon ablative heat shields as a form of thermal protection system (TPS) for future space access platforms. By predicting which areas of a vehicle's surface will experience the highest thermal loading, replaceable carbon ablative surfaces may be designed into the vehicle. After a sortie, the carbon ablator could be rapidly replaced and the vehicle could be prepared for its next mission.

Vehicle flight at hypersonic Mach numbers results in substantial heating to the forebody of the flight vehicle through convective and radiative heat flux transfer mechanisms. The radiative transfer of energy can represent a substantial portion of the overall flux to the surface of such a vehicle - accounting for as much as 60% or more of the total heat load in a blunt body [1]. This effect is not limited to blunt bodies however, but can also affect the stagnation region of narrower bodies, causing substantial heating and/or ablation to the nose tips of the thin vehicles. Due to the nature of hypersonic flow, even thin leading edges will become blunt at some point in the vehicle trajectory, thereby leading to increased radiation effects. Unfortunately, the solution of radiative heat transfer is a very complex area of study that is poorly understood and rarely utilized in the flowfield

solutions of most computational codes that are used to solve the flowfields of such vehicles. The effect of radiation is of particular concern for the US Air Force with increased emphasis upon the ability to have prompt, reusable launch vehicles (RLV). Radiation is always a concern in hypersonic vehicles, but the need to have reusable vehicles may require the use of replaceable TPS composed of ablative carbon materials, which presents interesting challenges for designers. Carbon is both a high emitter of radiation as well as a high absorber of radiation - therefore making the net effect highly variable, depending on the vehicle shape, velocity, and altitude. It is possible that carbon materials ablated at the nose of a vehicle could transport their energy downstream, where there is little or no thermal protection, in the form of internal energy modes and re-radiate the energy at locations downstream. This is possible even over narrow bodies that typically do not have significant radiative emission due to their shape. No "rule of thumb" can discard this possibility in an ablative environment.

Radiation, as a flowfield phenomenon, is complex for many reasons. One major difficulty is that radiation propagates at the speed of light, or virtually instantaneously in the computational domain of the average flight vehicle. The speed of propagation can be used to an advantage in computational simulation in that the radiative calculation can now be separated from the flowfield solution in a temporal sense. Radiation also propagates by line-of-sight, not flow direction, raising geometric difficulties for the code developer in accommodating radiative effects into the conventional grid-based flowfield solution methods since line of sight for each computational cell has to be determined. The thermophysical processes that lead to radiation also present a unique set of challenges. Radiation is a function of (T^4) - making accurate temperature determination a necessity in the flowfield. It is also very sensitive to which temperature is being considered if in a thermal nonequilibrium environment - the radiative bands in molecular radiation being dependent upon vibrational temperature, free-free electron radiation being a function of electronic temperature, etc. There is also a linear dependence of the radiation upon the species densities in the flowfield - radiation, and its adsorption, being not only a function of wavelength, but also which species is affected by which wavelength through quantum mechanics. This fact makes not only accurate species calculation important, but introduces

an additional degree of complexity in an ablative environment. Of particular concern is the effect of ablation with carbon species ablation shields since carbon is not only a strong absorber of radiation, but also a strong re-emitter of radiation.

1.1 Research Goals

The intent of this research is to develop a methodology by which a hypersonic flow solver, accounting for both thermal and chemical non-equilibrium, may be coupled with a spectral line-by-line radiation solver. It is desired that this solver be applicable to axisymetric bodies of arbitrary shapes and flowfields, with as few limiting assumptions as possible. One principal goal is to develop a method that is able to accurately predict the surface radiation imposed by a non-uniform radiation field.

It is desired that the model developed in the study be as accurate as possible with regards to the vibrational energies inherent to each chemical species. To this end, the model will handle multiple species vibrational energies, which will be used to determine the radiation properties of the gas.

Nearly all previous radiation work in this field has relied on the tangent-slab assumption, which assumes that the radiating gas near the vehicle's surface closely resembles a uniform infinite slab. Since the vehicles of interest to the Air Force are unlikely to have uniform flowfields, it is desired that a radiation propagation method be developed that does not rely on the tangent-slab assumption. The developed method will be able to accurately predict the radiative transport of energy in non-uniform flowfields.

Finally, the models developed in this work shall serve as the basis for a future project, wherein the radiation and flowfield calculations are carried out in a coupled fashion. This future work will include all chemical species of interest for an ablative earth re-entry.

1.2 Document Organization

- Chapter two will provide an overview of previous research in this area and relevant flight experiments.

- Chapter three will cover the relevant background and theory for hypersonic re-entry flows and radiation in a participating media.

- Chapter four will discuss the solution methodology.

- Chapter five will present results and their comparison with available flight data.

- Chapter six will provide recommendations for future work in this topic area.

2. PREVIOUS STUDIES AND EXPERIMENTS

This chapter will review related studies in the area for radiation - flowfield coupling. These studies will include both recent research, as well as earlier flight experiments.

2.1 Prior Research

There have been several attempts over the last few decades to couple radiative effects into flowfield codes. Most attempts have been done on a very simplified level with equilibrium models. One notable exception to this is the LORAN code of Hartung [2]. Hartung's work represented a triple hybridization in that it used the flowfield solution method of Gnoffo's LAURA [3] code with the nonequilibrium state population calculation method of Park [4], with Nicolet's RAD/EQUIL code for radiative heat transfer calculations. The LAURA code uses Park's [4] two-temperature model for thermal nonequilibrium, and a complete air-chemistry set for chemical non-equilibrium. In the LAURA implementation of the temperature model, one temperature is used to describe the heavy-particle energy of all molecules (T), while another temperature is used to describe the vibrational energy of molecules (T_v). The two temperatures are geometrically averaged to determine an average temperature (T_{ave}) used for chemical rate determination:

$$T_{ave} = \sqrt{TT_v} \tag{1}$$

The LAURA implementation of two-temperature model is limited in that it yields a single average heavy particle and vibrational temperature for all species in a cell. The goal of the LORAN code was to provide a relatively fast coupled solution method for design and analysis of hypersonic vehicles. To date, the code represents the "state-of-the-art" for coupled flowfield solution methods. Unfortunately, as personnel budget demands at NASA changed, the code has not been maintained, nor further development achieved since the mid-1990's.

While few production codes are in development, there has been a recent resurgence in NASA and academia in research codes examining methods of coupling radiation to

hypersonic flow solvers [1, 5, 6, 7, 8, 9, 10, 11]. Most of these recent endeavors involve either incorporation of, or comparison to, the line-by-line radiation code NEQAIR [12] with one of several flow solvers. Two flow solvers seeing extensive study are LAURA and DPLR [1, 6, 8, 9]. Both of these flow solvers have one lumped vibrational temperature for all of the diatomic species in the a computational cell. The two solvers also vary in their treatment of both the temperature characterizing the free electrons in the flow (electron temperature), and the temperature used to describe the electronic excitation of the gas (electronic temperature). In LAURA, both the electron and the electronic temperatures are assumed to be equilibrated with the vibrational mode. In DPLR the electronic temperature is neglected, assuming all of the electrons are in their ground state. DPLR does not have an explicit electron temperature, and various researchers have assumed that it is equivalent to either the translational temperature, or the rotational temperature.

Johnston et al. [9] have recently published works coupling radiation calculations into ablative flowfields around the Apollo 4 vehicle using a 22-species variant of the LAURA code coupled with the HARA (High-temperature Aerothermodynamic RAdiation) code. Johnston et al. determined that the inclusion of ablative species into the radiative analysis had a significant impact on the radiation that reached the vehicle surface. Furthermore, they also determined that the influence of the ablation products was highly dependent on both their concentrations and temperatures. The HARA code used in this study uses a tangent-slab approximation, which assumes that the radiative environment is uniform and does not vary significantly around the vehicle. The tangent-slab model will be discussed in detail in Chapter 3.

Feldick et al. [6] coupled DPLR with their own line-by-line spectral radiation solver to determine coupled heating rates for the Stardust vehicle. The geometry of the Stardust vehicle is given in Figure 1. Here again, the tangent slab approximation is used to determine the total radiative flux in any given cell. Feldick et al. determined that a vast majority of the computational effort in a coupled solution is spent performing the radiation calculation, approximately 98%. They also noted changes in shock stand-off distances, and radiative flux at the wall.

Wright et al. [1] used DPLR to examine radiative heating on a generic Titan entry capsule and the effects of coupling radiation. The Titan concept geometry used in this study is also shown in Figure 1. For the Titan atmosphere, Wright et al. showed that coupling the radiative heat flux into the flowfield solution reduced the shock stand-off distance, resulting in much lower predicted radiation intensity at the stagnation point. In this study, Wright et al. determined a correction to the tangent-slab radiation solution based on the view factors of each surface panel to the shock. This method resulted in lower radiative heating in general.

(a) Stardust, from [5]   (b) Titan, from [1]
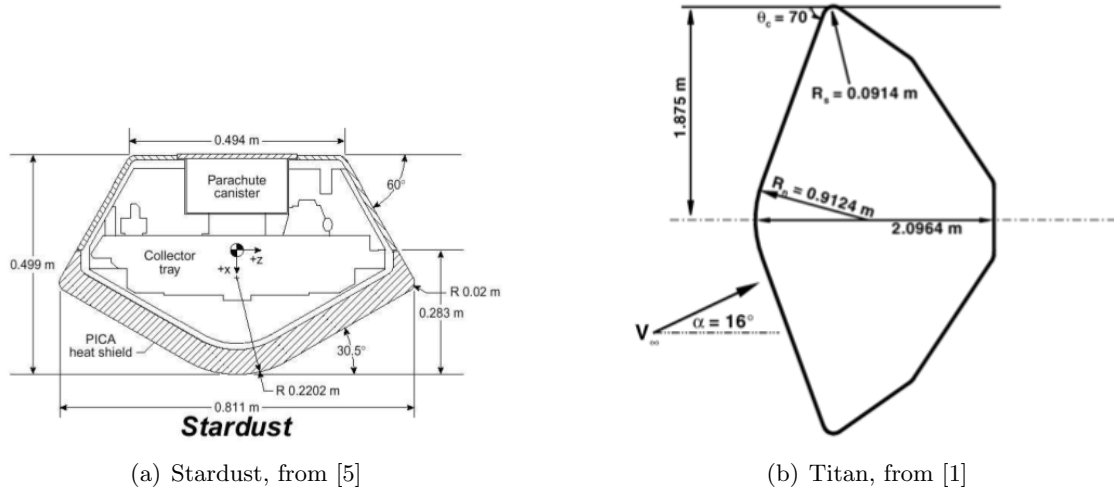
Figure 1   Contemporary hypersonic vehicle geometries

Most of the coupling methodologies used in these studies, involve the assumption of a large degree of uniformity of the radiation field via the tangent slab approximation. While this assumption is appropriate for the blunt bodies used in these studies, it may be entirely inappropriate for flowfields around narrow bodies.

2.2   FIRE-II Flight Experiment

On May 22nd, 1965, NASA launched its second experiment in Project FIRE [13]. This experiment, also known as FIRE-II, was intended to replicate the the heating environments that were expected to be experienced by space vehicles on lunar return trajectories. The experiment re-entered the earth's atmosphere at approximately 11.4 km/s. The flight

speed and trajectories were designed to ensure that the vehicle experienced appreciable radiative heating. A sketch of the vehicle is given in Figure 2
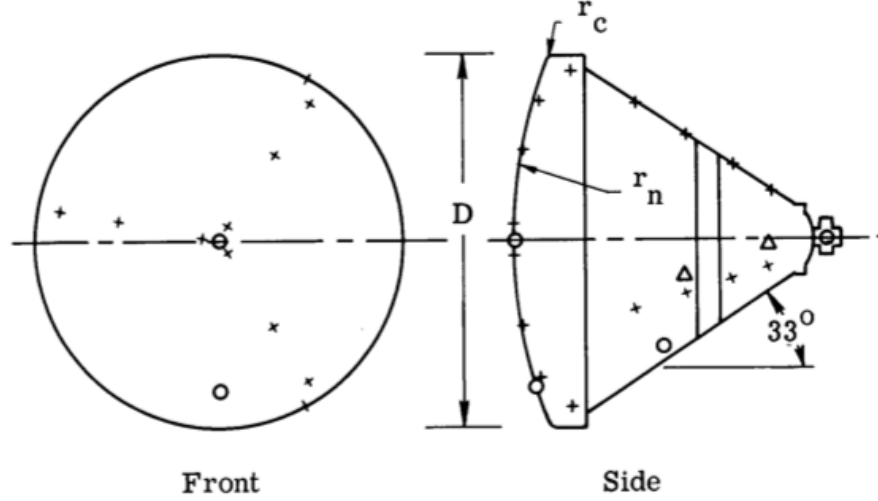
Figure 2   Sketch of FIRE-II from [14]. Circles denote radiometer placement

To record the radiative phenomena, the vehicle was well instrumented with three total radiometers, and one spectral radiometer [14]. One total radiometer was positioned on the stagnation line of the vehicle, another 16 to 20 degrees off the stagnation line, and the final one was located on the after-body of the vehicle. The optics for the stagnation line total radiometer were shared with the one spectral radiometer carried on the flight. The total radiometers in the experiment were sensitive to radiation in the 2,000 Angstrom to 40,000 Angstrom ($0.2\mu m$ to $4.0\mu m$) band. The spectral radiometer measured radiation in the 3,000 Angstrom to 6,000 Angstrom ($0.3\mu m$ to $0.6\mu m$) band, with a spectral resolution of 40 Angstrom ($0.004\mu m$).

In addition to the radiation measurements, total heating measurements were made with 12 calorimeter plugs arranged along three rays on the windward side of the vehicle [15]. These calorimeters measured the combined radiative and convective heat load. By differencing the calorimeter and radiometer measurements, the convective heat load can be calculated, along with the radiative heat load below 2,000 Angstrom ($0.2\mu m$), by:

$$Q_{cal} - Q_{R0.2 \to 4.0} = Q_{conv} + Q_{R0.0 \to 0.2} \tag{2}$$

8

One limitation of the experiment was the inability to measure radiation in the vacuum-ultraviolet (VUV) bandwidths. VUV radiation occurs below 2,000 Angstrom, and was entirely attenuated by the radiometer windows in the FIRE-II experiment. Even though radiation in the VUV region could not be directly measured, it was expected that VUV radiation be a significant contributor to the FIRE-II total heat load. Additionally, it is strongly suspected that the radiation measurements in the FIRE-II experiment were contaminated by the influence of ablation products. Despite these limitations, the FIRE-II experiment is the authoritative data-set for atmospheric radiation in earth reentry, and is used to this date in nearly all research into atmospheric radiation. [8, 10, 11, 16, 17]

3. RADIATIVE TRANSPORT THEORY

Background is presented in this chapter on the fundamental mechanisms of radiation in high temperature gases. Presented here will be pertinent phenomena and trends. For further detail, the reader is referred to the texts of Zel'dovich and Raizer [18], Modest [19], and the SPRADIAN user's manual [20].

3.1   Atomic Radiation

When considering an atomic gas at high temperatures, the radiation processes of the gas are driven by changes in the electrical states of the atoms, as shown in Figure 3. These radiation processes can be lumped into three categories: free-free transitions, bound-free transitions, and bound-bound transitions.
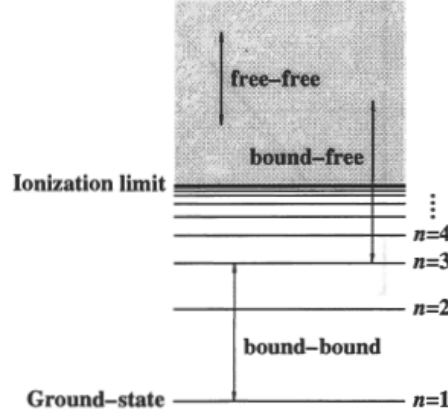
Figure 3   Electrical transitions leading to the emission of a photon, from [20]

For typical re-entry flows, the hot gas in the shock layer has a high degree of dissociation. As such, atomic radiation mechanisms play an important part of the overall radiation emission of the gas. As will be discussed below, atomic transition are characterized by strong lines of emission and absorption in the spectra. The presence of these lines make it very important that any modeling of spectral radiation be refined enough to accurately resolve these atomic lines.

3.1.1   *Free-Free Transitions.*   The first category considered is free-free transitions, wherein a free electron in the gas interacts with both ionic and neutral atoms. [18] Radi-

ation is emitted as the free electron is slowed due to its interactions with the ion's electric field, or through collisions with neutral particles. Due to the fact that the electron is able to lose virtually any amount of kinetic energy in this interaction, the radiation emitted by the interaction is continuous.

Free-free interactions are generally described by the following reaction [20]:

$$A^z + e_l + h\nu \leftrightharpoons A^z + e_u \tag{3}$$

where A^z is a heavy particle with z-valence, e_l and e_u are free electrons in lower and upper kinetic energy states respectively, and $h\nu$ is the photon. If the electrons are assumed to have a Maxwell-Boltzmann velocity distribution, then the above reaction can be assumed to be in equilibrium and the emission coefficient and absorption coefficients of this transition can be related using Kirchhoff's law.

$$\kappa(\lambda) = n^z n_e \sigma_{ff}^{z-1}(\lambda, T_{el}) \left[1 - \exp\left(-\frac{hc/\lambda}{kT_{el}} \right) \right] \tag{4}$$

$$\varepsilon(\lambda) = \frac{2hc^2}{\lambda^5} n^z n_e \sigma_{ff}^{z-1}(\lambda, T_{el}) \exp\left(-\frac{hc/\lambda}{kT_{el}} \right) \tag{5}$$

where σ_{ff}^{z-1} is an integrated electron velocity distribution, T_{el} is the temperature of the electrons, k is Boltzmann's constant, h is Planck's constant, c is the speed of light, and λ is the wavelength of the radiation being considered.

3.1.2 Bound-Free Transitions. Bound-free transitions are characterized by an electron changing states in one of two specific ways. The first state change involves the capture of a free electron along with the emission of a photon. This process is similar to the free-free transition, in that a free electron is decelerated due to the presence of an ion's electric field. If the electron loses enough energy through radiation to place it into a stable

11

orbit in one of the atom's electron shells, it will be captured. This process is also known as "radiative combination" [19].

The other state change considered involves the absorption of radiant energy by an atom with electron in high energy states. Should the energy absorbed by the electron exceed the ionization limit, the electron will leave its orbit and become a free electron in the gas. This process is also known as "photo-ionization."

The bound-free transition is described by the following reaction [20]:

$$A_l^{z-1} + h\nu \leftrightharpoons A_u^z + e \tag{6}$$
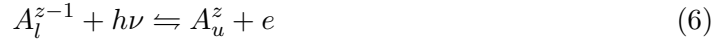
The rate of the reverse reaction (radiative combination), will be determined by the number density of heavy particles (A_u^z), the number density of free electrons with the appropriate amount of energy to participate in the reaction, a characteristic cross-section of the reaction, and the relative velocity of the electrons against the heavy particle. Combining these factors, the emission coefficient due to the bound-free transition is:

$$\varepsilon_{ul}(\lambda) = n_u n_e \frac{h^4 c^2}{(2\pi m_e k T_{el})^{3/2}} \frac{g_l}{g_u} \frac{\sigma_{lu}(\lambda)}{\lambda^5} \exp\left(-\frac{hc/\lambda - I_{ul}}{kT_{el}}\right) \tag{7}$$

where σ_{lu} is the Bound-free cross section for the reaction, m_e is the mass of an electron, and g is the degeneracy ratio of a given state.

Examined at equilibrium, and accounting for spontaneous emission, the net emission coefficient of the bound-free transition is:

$$\varepsilon_{ul}(\lambda) = \frac{2hc^2}{\lambda^5} n_u \sigma_{lu}(\lambda) \exp\left(\frac{hc/\lambda}{kT}\right) \tag{8}$$

The rate of the forward reaction (photo-ionization) is similarly determined by the number density of the heavy particle A_l^{z-1}, the intensity of the radiation $h\nu$, and the appropriate cross-section. In this case, a reduction factor must also be considered to

account for the effect of induced emission, which will lessen the net rate of the forward reaction. The net absorption coefficient is:

$$\kappa_{lu}(\lambda) = n_l \sigma_{lu}(\lambda)(1 - R_{bf})$$ (9)

The reduction factor due to spontaneous emission R_{bf} is given by:

$$R_{bf} = \exp\left(-\frac{hc/\lambda}{kT}\right)$$ (10)

The above relations for the emission and absorption coefficients of the bound-free transitions are applicable to individual transitions from a specific lower state to a specific upper state. The total emission and absorption coefficient would be the summation of the coefficients over all applicable state transitions.

3.1.3 Bound-Bound Transitions. Bound-bound transitions are entirely characterized by changes in electrical states within an atom. Electrons in high energy states may fall to a lower state through the emission of a photon. Similarly, an electron in a low energy state may be elevated to a higher energy stated after absorbing a photon. Because electrons can only exist at discrete energy levels in a given atom, the amount of energy emitted or absorbed in these transitions is similarly discrete. The discrete energy levels involved in these transitions lead to radiation characterized by strong spectral lines of emission and absorption. The strong lines of emission is contrasted with the semi-continuous spectra associated with bound-free and free-free transitions.

The reaction describing the bound-bound transition is [20]:

$$A_l + h\nu \leftrightharpoons A_u$$ (11)

The rate of the reverse reaction will be proportional to the number density of heavy particles A_u, and the probability of a transition occurring. The emission coefficient can therefor be described as:

$$\varepsilon(\lambda) = n_u \frac{hcA_{ul}}{4\pi\lambda_{ul}}\Phi(\lambda) \tag{12}$$

where A_{ul} is the Einstein A coefficient for the transition probability of spontaneous emission, and Φ is a line broadening term. The Einstein A coefficient describes the probability that a particle in a given excited state will spontaneously transition to a lower state, and in the process emit a photon. These coefficients are well characterized, and available in SPRADIAN. The line broadening term is applied to account for the doppler effect as particles with very high translational speeds emit and absorb while traveling in different directions. The forward rate of the reaction is similarly governed by the number density of the heavy particle A_l, and the intensity of the radiation $h\nu$. The rate will be attenuated by the induced emission at this frequency, which is also proportional to these two factors. The expression for the overall absorption coefficient is:

$$\kappa(\lambda) = \frac{h\lambda_{ul}}{c}(n_l B_{lu} - n_u B_{ul})\Phi(\lambda) \tag{13}$$

where B_{lu} is the Einstein coefficient for induced absorption, B_{ul} is the Einstein coefficient for induced emission, and again Φ is a line broadening term. Using known relations for the Einstein B coefficients and the Einstein A coefficient, the net absorption coefficient may be written as:

$$\kappa(\lambda) = n_l \frac{A_{ul}\lambda_{ul}^4}{8\pi c}\frac{g_u}{g_l}\left(1 - \frac{n_u g_l}{n_l g_u}\right)\Phi(\lambda) \tag{14}$$

As with the bound-free transitions, the total bound-bound emission and absorption coefficients are determined by a summation over all probable transitions. It is also possible for induced emission to occur at a rate greater than induced absorption. This behavior, also known as lasing, is indicated by the absorption coefficient being negative.

3.2 Molecular Radiation

Radiation processes in molecules differ slightly from radiation processes in atoms due to the nature of their respective energy storage modes. The internal energy of an atom is solely determined by its electronic state, while a molecule's internal energy is determined by its electronic state in addition to the level of excitation of its vibrational and rotational modes [18].

Similar to bound-bound transitions, the transitions of internal energies of a molecule are also discrete. Unlike bound-bound transitions, there are a vast number of discrete internal transitions that result in changes of energy that are very close to one another. The result is that emission and absorption of radiation from molecular systems form bands of similar vibrational-rotational-electrical energies. The fundamental wavelength of any band will largely be determined by the change of vibrational energy associated with the particular class of transition, since the energy quanta needed to change a vibrational state is much larger than the quanta needed to change a rotational state. However, the inclusion of all of the probable rotational transitions associated with the primary vibrational transition leads to many closely spaced spectral lines [19].

Molecular radiation is of interest for hypersonic flows for three reasons. First, many transient molecular species are highly radiative, meaning that even trace concentrations of these species may have a significant impact on the radiation field around a vehicle. Second, the continuous nature of molecular radiation may lead to very large intensities when the radiation is integrated over all wavelengths. Finally, the hypersonic boundary layer usually consists of relatively cool molecular gases, which form an insulating absorption layer near the surface of the vehicle.

The general reaction for the molecular transition may be written as:

$$A_{J',v',e'} + h\nu \rightleftharpoons A_{J'',v'',e''} \tag{15}$$

The forward reaction involves the absorption of a photon, and the transition of internal states from J', v', e' to J'', v'', e''. Einstein A coefficients do exist for a number of these likely transition for elements of air chemistry. The data set is not as complete, however, as it is for the atomic transitions due to the vast number of possible molecular transitions.

3.3   Flowfield Coupling

For the radiation properties of a gas to be of any use to an aerodynamicist, there needs to be some model to incorporate the radiation field with the flowfield, ultimately resulting in a determination of the convective and radiative heat fluxes to the surface of the vehicle in consideration. Two traditional radiation propagation models are presented in this section.

3.3.1   Tangent Slab Model.   The simplest, and most common, approximation used for geometric considerations in radiation modeling is to assume that the layer of radiating gas in front of the vehicle approximates a uniform two-dimensional slab. If the shock layer has a thickness much less than the radius of curvature of the vehicle, then the radiation field closely approximates the tangent slab assumption. For the purpose of analysis, the surface is treated as being an infinite flat two-dimensional surface. The radiating gas layer is assumed to be uniform across the entire surface of the slab, varying in the wall normal direction only. Figure 4 describes the geometry of the tangent-slab approximation. Fujita and Abe [20] develop the equations for the tangent-slab as follows:

Start by defining a small volume element of radiating gas

$$\mathbf{dr} = r^2 \sin\theta \, dr \, d\theta \, d\psi \tag{16}$$

Then determine the solid angle Ω between the differential surface dS and the volume $\mathbf{dr}$

16
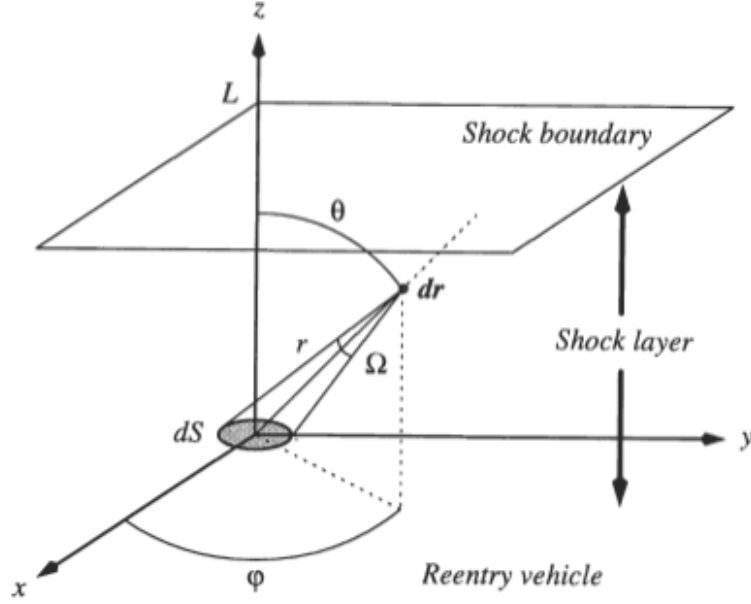
Figure 4   Tangent Slab Geometry from [20]

$$\Omega = \frac{\mathbf{dS} \cdot \mathbf{r}/r}{r^2} = \frac{dS cos\theta}{r^2} \tag{17}$$

The total radiation power emitted from the the volume $\mathbf{dr}$ into the solid angle Ω is

$$\varepsilon(\mathbf{r})\mathbf{dr}\Omega = \varepsilon(\mathbf{r}) \sin\theta \cos\theta dr d\theta d\psi dS \tag{18}$$

The gas between the emitting element and the surface is a participating media. This layer both absorbs and emits radiation. The radiative intensity along the ray from dS and $\mathbf{dr}$ follows from the radiative transport equation (RTE):

$$\frac{dI_\lambda}{dx} = \varepsilon - \kappa' I_\lambda \tag{19}$$

Solving the RTE using Equation 18 as a boundary condition on the radiative intensity at the origin, and neglecting the emission between the two points, we can determine the power transfered from $\mathbf{dr}$ to the surface dS:

$$dP = \varepsilon(\mathbf{r}) \sin\theta \cos\theta dr d\theta d\psi dS \times \exp\left[-\int_0^r \kappa'(\mathbf{r}')dr'\right] \tag{20}$$

By the assumption of the uniformity of the slab, radiative properties are a function of distance from the wall only. Therefore, we can apply the following relations:

$$\kappa'(\mathbf{r}') = \kappa'(z') \tag{21}$$

$$dz' = dr' \cos\theta \tag{22}$$

Further, defining the effective optical depth as:

$$K(z) \equiv \int_0^z \kappa'(z')dz' \tag{23}$$

we can rewrite the integral portion of Equation 20 as

$$\int_0^r \kappa'(\mathbf{r}')dr' = \int_0^z \frac{\kappa'(z')}{\cos\theta}dz' = \frac{K(z)}{\cos\theta} \tag{24}$$

Integrating Equation 20 over the entire shock layer and applying another transformation from $\mathbf{r}$ to z:

$$P = \iiint \varepsilon(z) \sin\theta dz d\theta d\psi dS \times \exp\left[-\frac{K(z)}{\cos\theta}\right] \tag{25}$$

$$= 2\pi dS \int_0^{\pi/2} \sin\theta \int_0^L \varepsilon(z) \exp\left[-\frac{K(z)}{\cos\theta}\right] dz d\theta \tag{26}$$

The cosine term in the exponential indicates that for transmission along the wall, the radiation is highly absorbed. In the special case that the gas is lightly absorbed or optically thin ($K \to 0$), the exponential term becomes unity. In this case, the heat flux predicted by the tangent-slab model becomes:

$$q = \frac{P}{dS} = 2\pi \int_0^L \varepsilon(z)dz \qquad (27)$$

Further, if the emission is homogenous, the heat flux is simply:

$$q = 2\pi\varepsilon L \qquad (28)$$

In practice, most implementations of the tangent-slab model numerically integrate the RTE (Equation 19) from the shock edge to the surface of the vehicle. To solve the RTE, the emissivity and absorptivity of the gas is assumed to be piece-wise linear between the two points of integration, as follows:

$$\varepsilon = \varepsilon_0 + ax \qquad (29)$$

$$\kappa = \kappa_0 + bx \qquad (30)$$

The heat flux at the surface is then determined assuming a uniform integration

$$q_r = 2\pi I_w \qquad (31)$$

The relations for the tangent-slab model were all developed based on the assumption that the radiating shock layer is approximated by a uniform slab of radiating gas. The only variation allowed in this assumption is in the wall normal direction.

3.3.2   Gas Cap Model.   Fujita and Abe [20] also present the development of uniform radiation solution in a spherical coordinate system. In this spherical gas cap model, the curvature of the vehicle and the curvature of the shock are taken into account. Like the tangent-slab model, the radiation field is assumed to be uniform in all directions, and only vary with the distance from the body. A diagram of the model from [20] is presented in Figure 5:
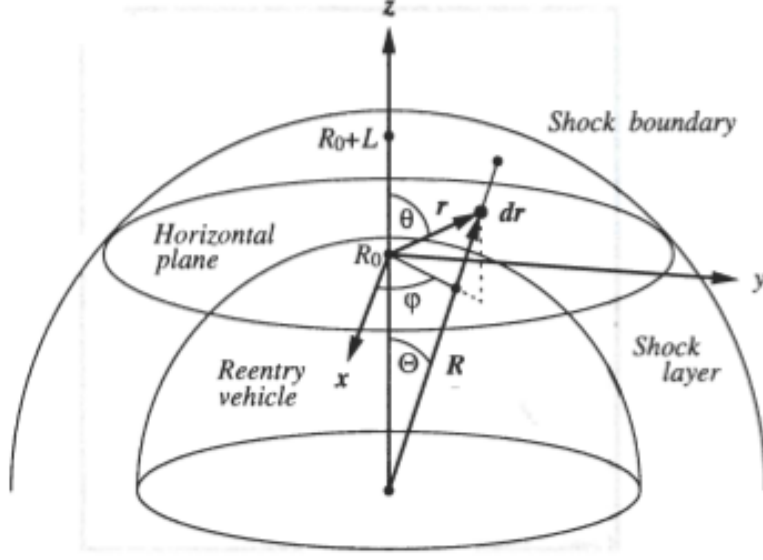
Figure 5   Gas Cap Geometry from [20]

For this geometry, we can use Equation 20 as previously stated. It will, however, be more convenient to work in a spherical frame of reference from the axis of symmetry, R. The two are related as follows:

$$dr = \frac{RdR}{\sqrt{R^2 - R_0^2 \sin^2 \theta}} \tag{32}$$

As was done in the case of the tangent slab, the assumption of the uniformity of the gas layer allows us to change the radiative properties of Equation 20 into our R frame using $\varepsilon(\mathbf{r}) = \varepsilon(R)$ and $\kappa'(\mathbf{r}) = \kappa'(R)$. This transformation yields the following expression for the power received at the stagnation point from a radiating element:

$$dP = \varepsilon(R) \sin\theta \cos\theta \frac{RdR}{\sqrt{R^2 - R_0^2 \sin^2 \theta}} d\theta d\psi dS \times \exp\left[-\int_{R_0}^{R} \frac{\kappa'(R')R'dR'}{\sqrt{R'^2 - R_0^2 \sin^2 \theta}}\right] \tag{33}$$

Acknowledging the symmetry of the problem, and integrating over the hemisphere, the total heat flux at the stagnation point becomes:

20

$$q = \pi \int_0^{\pi/2} \sin 2\theta d\theta \int_{R_0}^{R_0+L} \frac{\varepsilon(R)RdR}{\sqrt{R^2 - R_0^2 \sin^2 \theta}} \exp\left[-\int_{R_0}^R \frac{\kappa'(R')R'dR'}{\sqrt{R'^2 - R_0^2 \sin^2 \theta}}\right] \qquad (34)$$

Finally, we have arrived on analytic expressions for the radiative heat flux incident on the surface of a uniform slab (Equation 25) and the stagnation point of a uniform spherical gas cap (Equation 34). These expressions are straight forward to solve numerically, however they both come with an important assumption; the radiation properties of the gas are assumed to vary in one direction only.

4. SOLUTION METHODOLOGY

The following method was used to determine the flowfield and radiation properties used for this research. The flow code and radiation code have been integrated, but are run in an uncoupled fashion. A converged flowfield is generated by the flowfield portion of the code. Once the flow has converged, the species concentrations, heavy particle temperature, and the species vibrational temperatures are passed as inputs to the radiation portion of the code. For all geometries used in this study, a flowfield resolution of 50 cells in the i-direction, and 60 cells in the j-direction was used.

4.1 Detailed Tracking of Vibrational Temperatures

For the purposes of this study, a seven-species air chemistry model with one ionized species was used. The flow solver NH7Air [21] was selected due to its ability to independently track the vibrational energy of diatomic species in the flow. Knowledge of species-specific vibrational energy allows for very precise energy calculations, particularly when considering radiative emission and absorption. The NH7Air flow solver is a finite volume, Roe approximate Riemann solver. The solver is second-order accurate through the employment of a MUSCL method, with a minmod limiter reducing the accuracy to first-order in the vicinity of strong shocks. The solver evaluates viscous flux terms using central differencing. A time-explicit predictor-corrector method is used in the solver. The solver assumes that translational and rotational energy modes are in thermodynamic equilibrium, while independently tracking the vibrational energy mode of each diatomic species and the energy associated with the free electrons. A separate species energy equation is used to determine the energy of the diatomic species and the free electrons. The chemical species considered by the code are: N_2, O_2, N, O, NO, NO^+ and e^-. A detailed discussion of the solver is presented in Ref [21]. An overview of the solver's development is presented below:

4.1.1 Species Mass Conservation. The species mass conservation is given by

$$\frac{\partial}{\partial t}\rho_s + \frac{\partial}{\partial x^j}\rho_s u^j = \frac{\partial}{\partial x^j}\left(\rho_s V_s^j\right) + \dot{\omega}_s \tag{35}$$

where the diffusion velocity of species s is given by:

$$V_s^j = u_s^j - u^j \tag{36}$$

The term $\dot{\omega}_s$ represents the rate of species creation and destruction, whose sum over all species is zero.

$$\sum_s \dot{\omega}_s = 0 \tag{37}$$

Similarly, the sum of mass flux due to diffusion is also zero.

$$\sum_s \rho_s V_s^j = 0 \tag{38}$$

The dissociation rates were determined using a functional form of the Arrhenius equation:

$$k_f(T_{\text{eff}}) = C_f T_{\text{eff}}^{\eta} e^{\theta_d/T_{\text{eff}}} \tag{39}$$

where the effective temperature, T_{eff} is determined using the two-temperature model.

$$T_{\text{eff}} = \sqrt{TT_{v,s}} \tag{40}$$

4.1.2 Total Momentum Conservation.

The total momentum conservation is given by

$$\frac{\partial}{\partial t}(\rho u^i) + \frac{\partial}{\partial x^j}(\rho u^i u^j) + \frac{\partial P}{\partial x^i} - \frac{\partial \tau^{ij}}{\partial x^j} = \sum_s n_s e_s Z_s E^i \tag{41}$$

The right hand side of the preceding equation accounts for the electric effects upon the flowfield, with E^i representing an approximation of the electric field.

4.1.3 Total Energy Conservation.

The equation used to enforce the conservation of total energy is

$$\frac{\partial}{\partial t}\left[\rho\left(\frac{1}{2}u^2 + e\right)\right] + \frac{\partial}{\partial x^j}\left[\rho u^j\left(\frac{1}{2}u^2 + e\right)\right] + \frac{\partial q^j}{\partial x^j} + \frac{\partial}{\partial x^j}(u^j P) - \frac{\partial}{\partial x^j}(u^i \tau^{ij}) = \sum_s \epsilon N_s Z_s E^i u_s^i \tag{42}$$

where the term on the right-hand side of the equation is the work done on the electrons by the electric field.

4.1.4 Vibrational Energy Conservation Equation.

The vibrational energy of each diatomic species is determined by

$$\frac{\partial}{\partial t}(\rho_s e_{v,s}) + \frac{\partial}{\partial x^j}\left(\rho_s e_{v,s} u^j\right) = \underbrace{\frac{\partial}{\partial x^j}\left(\eta'_{v,s}\frac{\partial T_v}{\partial x^j}\right)}_{1} - \underbrace{\frac{\partial}{\partial x^j}\left(\rho_s e_{v,s} V_s^j\right)}_{2} + \underbrace{Q_{T-V}}_{3} + \underbrace{Q_{e-V}}_{4} + \underbrace{\dot{\omega}_s D_s}_{5} \tag{43}$$

In this equation, the first term accounts for the conduction of species vibrational energy. The second term accounts for the diffusion of species vibrational energy. The third and

24

fourth terms account for the energy transfer between modes. The final term accounts for the vibrational energy associated with the creation or destruction of of the species.

The solver's treatment of vibrational energy in a manner that is specific to each species is unique, and was a determining factor in its selection for this study. The species energy equations allow for the exact determination of the vibrational temperature of each species. It also allows for the potential inclusion of a radiative source term, which would be an entry point to coupling the flowfield with a radiative solver. Once species specific contributions to the radiative field are known, the species radiative heat transfer is introduced to balance the energy equation, as follows:

$$\frac{\partial}{\partial t}(\rho_s e_{v,s}) + \frac{\partial}{\partial x^j}\left(\rho_s e_{v,s} u^j\right) = \frac{\partial}{\partial x^j}\left(\eta'_{v,s}\frac{\partial T_v}{\partial x^j}\right) - \frac{\partial}{\partial x^j}\left(\rho_s e_{v,s} V_s^j\right) + Q_{T-V} + Q_{e-V} + \dot{\omega}_s D_s + Q_{R,s}$$

(44)

The second appendix of the PhD thesis of Hartung [2] includes finite volume formulations of the radiative source term.

4.2   Grid Adaptation

In a hypersonic flow, the flow field is homogenous up stream of the shock. Therefore, the goal of grid adaptation is to adjust the grid such that a minimum number of cells are placed upstream of the shock, while simultaneously clustering cells at the shock and maintaining appropriate viscous spacing at the wall. Grid clustering near the wall is desirable in order to capture and resolve the viscous boundary layer around the hypersonic vehicle. Grid clustering near the shock is desirable so that sufficient spacial resolution is present in the part of the flowfield that experiences the strongest gradients, and the largest degree of thermo-chemical non-equilibrium. For a short distance past a hypersonic boundary layer, vibrational modes and chemical rates have not yet equilibrated with the translational motion of the molecules, therefore an increased resolution is desired to accurately model these effects.

The NH7Air code was modified to include the grid adaptation method of Gnoffo et al. [22] This grid adaptation method performs a series of transformations to remap the existing grid into a smoothly varying grid that refines both the shock and boundary layer. First, a non-dimensional first cell height is defined by:

$$\Delta\hat{n}(1) = \frac{N_{Re_{\text{cell}}}\mu(1)}{\rho(1)a(1)n^{(1)}(K)} \tag{45}$$

where K is the number of cells in the ζ direction, and $N_{Re_{\text{cell}}}$ is the user specified first cell Reynolds number. The user specifies the fraction of cells to be used in the boundary layer via F_{bl}. The heights of the next K_{bl} cells is defined by:

$$K_{bl} = F_{bl}K \tag{46}$$

$$\Delta\hat{n}(k) = \left[1 + C\sin\left(\frac{(k-1)\pi}{K_{bl}-1}\right)\right]\Delta\hat{n}(k-1) \tag{47}$$

where

$$C = \left(\frac{F_{bl}}{\Delta\hat{n}(1)}\right)^{\frac{1}{K_{bl}}} - 1 \tag{48}$$

The spacing obtained at the edge of boundary layer, $\Delta\hat{n}(K_{bl})$, is held constant for the rest of the shock layer. The actual distribution is obtained from a summation of the increments.

$$\hat{n}(k+1/2) = \sum_{l=1}^{k}\Delta\hat{n}(l) \tag{49}$$

Another transformation is then applied to pull points to the user specified shock location, F_{sh}, to resolve the shock front.

$$\tilde{n}(k+1/2) = [1 - \epsilon(k+1/2)]\hat{n}(k+1/2) + F_{sh}\epsilon(k+1/2) \tag{50}$$

where

$$\epsilon(k + 1/2) = \hat{n}^2(k + 1/2)[1 - \hat{n}(k + 1/2)]\epsilon_0 \tag{51}$$

where the user specifies the clustering parameter, ϵ_0. This second transformation alters the distribution at the wall very little, while clustering points near F_{sh}. A final transformation returns dimensionality to the grid, while keeping the original shock location fixed.

$$n^{(1)}(k) = \frac{n^{(1)}(*)\tilde{n}(k)}{F_{sh}} \tag{52}$$

where $n^{(1)}(*)$ is the location in the original grid where the shock was detected. This process can be applied independently to each row of cells in the wall normal direction. Once the transformation is performed, a simple first-order interpolation/extrapolation is performed to map the flow variable to the new grid. Table 1 gives recommend values for the grid control parameters, as well as the values in this study.

Table 1   Recommended grid control parameters

Parameter	Recommended Gnoffo et al.	Used this study
$N_{Re_{\text{cell}}}$	1.0	15.0
F_{bl}	0.5	0.4
F_{sh}	0.8	0.7
ϵ_0	25/4	23/4

Grid adaptation was executed multiple times during the course of a computational run. A trial-and-error process was used to balance the number of cells used to refine the shock and boundary layers. The grids used in this study were generally coarser than those used by Gnoffo, so care had to be taken to balance the clustering and grid placement, without stretching the grid too much. In particular, a higher value of $N_{RE_{\text{cell}}}$ was used to produce a more gradual stretching rate of cells in the boundary layer. This grid adaptation method produces cells with extreme aspect ratios in the boundary layer, so care had to be taken to ensure that the finite volume flow solver remained stable.

4.3   Spatially Accurate Transport of Radiative Energy

The first required action in performing a radiation update to a flowfield is to determine the emission coefficient and absorption coefficient, by wavelength, throughout the domain. To perform this, the line-by-line radiation code SPRADIAN [20] was incorporated into the NH7Air solver. Pertinent information of the gas chemistry is passed to SPRADIAN for the determination of a given cell's excited state populations, and coefficients of emissivity and absorptivity. This information includes species number density, translational, vibrational, and electron temperatures, and radiation mechanisms of interest.

Once the radiation portion of the code has determined the emission and absorption spectrum throughout the flowfield, a radiation update is performed to determine radiative intensity at any point in the flowfield and on all surfaces. A tangent-slab or spherical gas-cap model could be used to determine the surface intensities. Inaccuracies would arise however, for geometries and flowfields that violated the geometric assumptions of these models. The primary assumption of concern is that the radiation environment is uniform with respect to angle as viewed from the surface.

A new radiation propagation algorithm is presented which does not assume that the radiation field is planar and uniform throughout the shock layer. The algorithm is two-dimensional in nature, and does not inherently take into account the effects of the third-dimension. There is therefore an implied assumption that the radiation field is axisymmetric. In this method, the RTE is solved directly in each cell from all neighboring cell taking into account a user specified number of transmission directions. This method is essentially one where a two-dimensional reference frame fixed in physical space is used to determine radiative transport for an arbitrary flow domain in ξ-η space.

When considering radiation propagation in two dimensions, emission from a cell is uniform in all directions. As emitted radiation is propagated throughout the domain, it will continue to travel in the direction in which it was emitted, attenuated by absorption and emission along its path. We can describe a two-dimensional circular coordinate system in physical space that is comprised of a number of transmission directions, shown in Figure 6. Emission from a cell will be the same in each of these transmission directions. The emitted

radiation will intersect neighbor cells, and result in a net radiative intensity in that cell. In this method, the RTE is solved directly assuming a linear variation of emission and absorption coefficients between the cell neighbors.
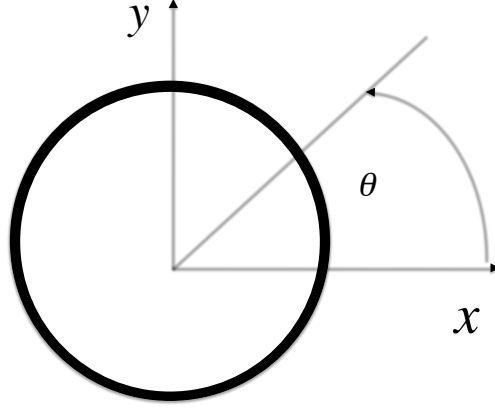
Figure 6   Coordinate system for radiative transport

Depending on the number of directions chosen to account for radiation propagation, there may exist cases where transmission in a given direction will intersect more than one neighboring cell. An example of this situation is shown in Figure 7. In these situations, a simple weighting is appropriate to accurately account for the influence of radiation in this direction on the neighbors. The weighting is determined by the ratio of the angular overlap of the transmission direction with the cell to the total angle of the transmission direction. A notional example is shown in Figure 7, where the red lines denote the edges of the transmission directions, and the blue line denote the angular extent of the neighboring cell.

4.3.1 Algorithm Details.   The details of the algorithm for the non-uniform radiation propagation method are presented below.

Figure 7   Overlap between transmission directions and cell neighbors

1. Invoke SPRADIAN to determine spectral emission and absorption coefficients in each cell. SPRADIAN has been modified to allow species-specific vibrational temperatures to be used in the radiation calculations.
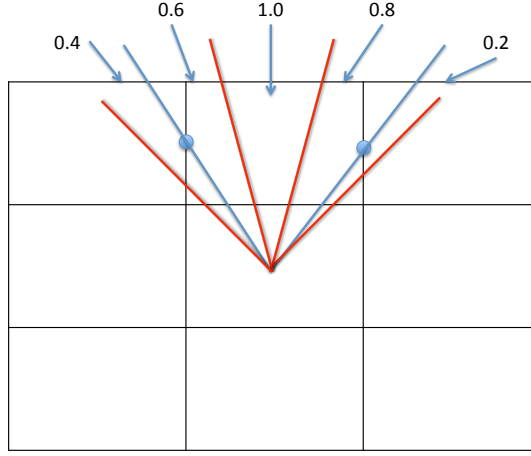
2. Choose a number of transmission directions, and determine the angular extent of each direction. In a traditional tangent-slab analysis, two transmission directions are considered; one towards the body and one away from the body. In this method, an arbitrary number of directions may be chosen, each of which equally share a 2π two-dimensional angle. For instance, if four transmission directions were chosen, each direction would cover a $\pi/2$ angular region. The minimum and maximum angle of each transmission direction is stored, and is later used to determine which transmission directions will intersect a given cell neighbor. The first direction is aligned with the $+x$ axis to ensure alignment with the vehicle's stagnation point.

3. Cycling over domain, determine the angle formed by the ray from all cell centers to the edge midpoint of each adjoining neighbor, as shown in Figure 8. These angles, combined with the angles defining the transmission directions, are used to determine

which angles of radiation propagation are going to intercept each neighbor. These angle are defined in the same physical space as the transmission directions.
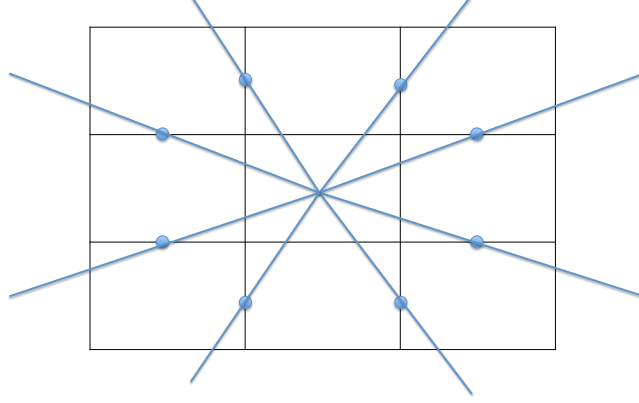
Figure 8   Determination of neighbor bounds

4. Cycling over each transmission direction, compare the minimum and maximum angles of the transmission direction to the minimum and maximum angles of the rays to the neighboring cell edges. If an overlap occurs, this indicates that emissions and transmitted energy from the center cell in that transmission direction will intersect a given number of neighboring cells. The extent of this overlap is the ratio of the angular extent of the overlap (α_{dir}) to the total included angle of the transmission direction (β). The dimensions needed to store this information are proportional to the number of cells in the domain, the number of transmission directions chosen, and the number of neighbors each cell has. This calculation is performed once upon initialization, and the coefficients are stored for later use.

$$c_{i,j \to i_n, j_n} = \frac{\alpha_{dir}}{\beta} \tag{53}$$

5. Update the radiation field through a series of alternating sweeps $(+i, +j)$ $(-i, -j)$ $(-j, +i)$ $(+j, -i)$. In each increment of the sweep, accomplish the following:

   (a) Initialize radiation intensity in wall-bounded cells using a grey-body distribution for all directions pointing away from the wall. This is the effect of radiation from the surface of the vehicle.

$$I_{w,\lambda} = 0.8 I_{bb,\lambda} \tag{54}$$

   (b) Computationally examine each neighboring cell. For each neighboring cell, cycle over all transmission directions. If the neighboring cell does not exist (edge of the domain), or if a given transmission direction from this neighbor does not overlap the center cell, then no update is made to the radiative intensity in the center cell. This check is performed using the previously stored view coefficient (Equation 53).

   (c) If an overlap exists between a transmission direction from this neighbor, invoke SPRADIAN to solve the RTE (Equation 55), assuming a liner variation of both emission coefficient and absorption coefficient. The intensity and emissivity of the neighboring cell are scaled by the view coefficient with this direction to the center cell. For example, if a transmission direction equally overlaps two cells, only half of the emissivity and intensity is used to calculate an updated intensity in each of those cells, thereby enforcing conservation of energy. The distance used the integration of the radiation propagation equation is the distance between cell centers.

$$\frac{dI_\lambda}{dx} = \varepsilon - \kappa I_\lambda \tag{55}$$

   The total intensity in the cell in each direction is determined by adding the contributions to radiative intensity in this direction from each neighboring cell.

$$I_{i,j,\lambda,dir} = \sum_{i_n,j_n} [I_{\lambda,dir}]_{i_n,j_n \to i,j} \tag{56}$$

6. Large arrays are required to store the spectral intensity information throughout the domain. The intensity must be stored at each wavelength in each direction within every cell. The memory required is proportional to the number of cells in the domain multiplied by the product of the number of transmission directions and the number of points in the spectrum.

7. To determine the radiative heat flux at the wall, a hemispherical integration is performed incorporating the radiative intensity for each direction that intersects the wall.

$$q_r = \int_0^{\pi/2} \int_0^{2\pi} I_{dir} d\phi d\theta \tag{57}$$

5. RESULTS

The two principle radiation fields that will be presented in this work are that of a uniform radiating slab, and that of the FIRE-II vehicle. The uniform radiating slab is examined to provide a direct validation of the radiation propagation method against the tangent-slab method. The FIRE-II case is examined to validate the combined flowfield - radiation solver.

5.1 Uniform Slab

Any radiation propagation calculation performed on a uniform slab of gas radiating to an infinite surface should return the same result as that of the tangent-slab model. For this reason, the uniform slab case is an important validation case for the non-uniform radiation propagation method. The grid used for the uniform slab case is given in Figure 9.
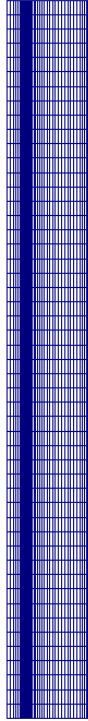

Figure 9   Grid used for uniform slab case

The right boundary of this grid is the surface receiving the radiative energy. The left boundary is the free stream, the top boundary is an imposed zero gradient condition, and

the bottom boundary is an axis of symmetry. The grid is clustered near the surface and near the shock front. A notional radiation field is imposed in this case, which varies only in the wall normal direction. An overview of the solver settings used for the radiating air chemistry are presented below:

Table 2   Radiation settings for uniform slab analysis

Chemical Composition	7-species Air
Spectral Range	2,000 Å - 15,000 Å
Spectral Resolution	0.13 Å
Number of Spectral Points	100,000
Number of Directions Considered	12, 16, 20

As a initial point of comparison, contours of wall-normal intensity are given in Figure 10. When considering radiation intensity in the wall normal direction, both methods result in similar intensities throughout the flowfield.

(a) tangent-slab   (b) non-uniform
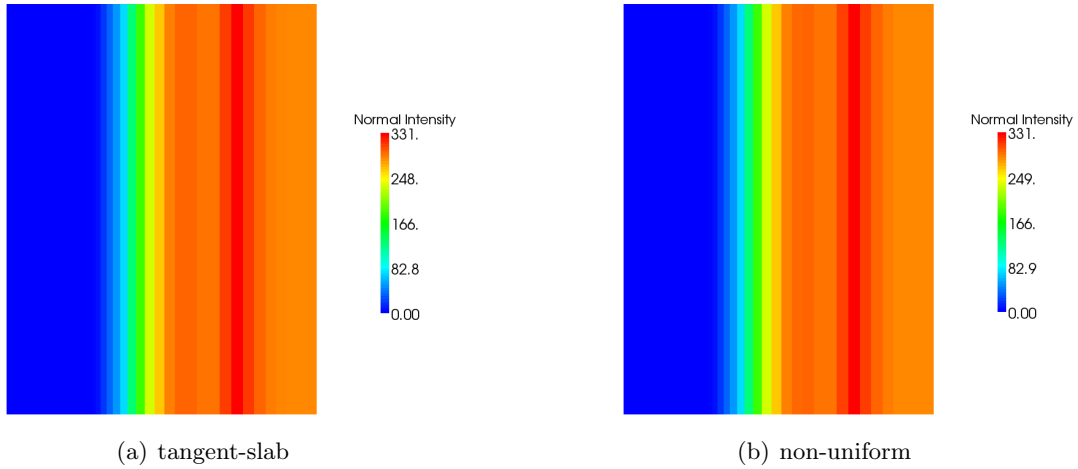
Figure 10   Wall normal intensity of uniform slab $[W/cm^2 - st]$

The uniform slab was examined with a varying number of radiation transmission directions. Two features that were examined to determine the non-uniform method's validity were: 1) prediction of uniform intensity across the surface, and 2) agreement with the intensities predicted using the tangent-slab model.

5.1.1 *Uniformity.*   With a uniform slab of gas radiating to an infinite plate, any radiation coupling method should predict uniform surface intensities, regardless of

the location on the plate. The method developed in this study was used to examine just such a case. The new method predicted uniform intensity regardless of the number of transmission directions, as is apparent in Figure 11. At all indexes along the plate the new method predicts the same surface intensity, within numerical precision.

Radiative Power vs Index
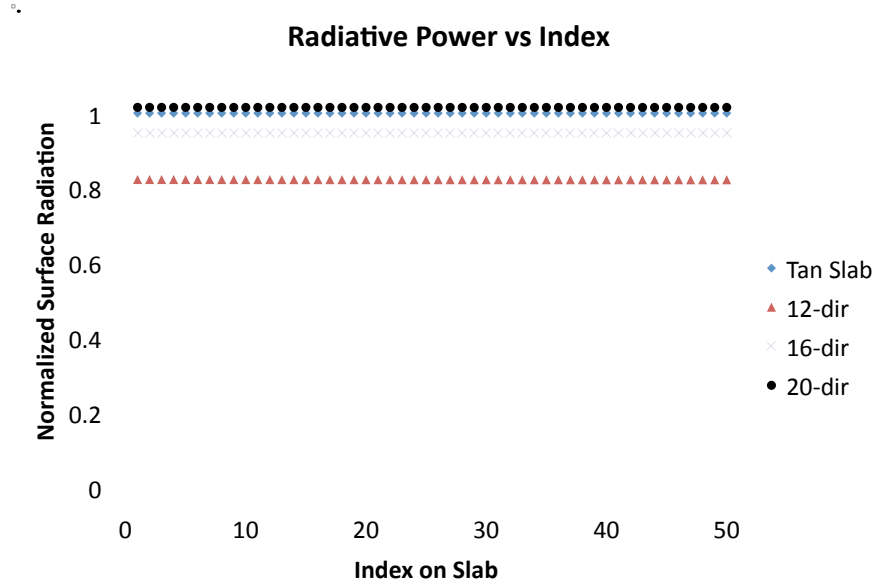
Figure 11   Uniform radiating slab intensities using a varying number of transmission directions

5.1.2   Comparison to the Tangent-Slab Model.   The agreement with the tangent-model is very good in this case, as can be seen in Table 3. The new method's agreement with with the tangent slab model increases as the number of transmission directions increases. Agreement is within approximately 5% when sixteen transmission directions are considered, and better than 2% when twenty transmission directions are considered.

Exact agreement is not expected in this case due to the absorption in the boundary layer. As was discussed in Chapter 3, a real radiating gas layer is highly absorbed for transmission directions that are nearly parallel to the wall. The traditional implementation

Table 3   Error at various number of transmission directions

Directions	Error(%)
12	17.8
16	5.4
20	1.6

of the tangent-slab model does not account for this, while the new method does. For this reason, we do expect the new method to slightly under predict the radiation intensity at the wall when compared to the tangent-slab model.

The model's behavior of increasing the predicted intensity with an increasing number of transmission directions can be explained in two ways. First, once the new method selects the neighbor pairing for a given transmission direction, it solves the RTE using the distance between the cell centers as the integration length. In a general sense this is appropriate, however the cells in the boundary layer complicate this integration. Because of the high aspect ratio of all cells in the boundary layer, most of the transmission directions will intersect neighbors in the wall normal direction. The method therefore, may be integrating over distances that are too short for the transmission directions that are not aligned with the wall normal. Since any real boundary layer is highly absorptive, the effect of the shorter integration will be higher predicted intensities at the wall. Second, the hemispherical integration performed at the wall is, in effect, a banded weighting of all of the transmission directions into the wall. As the number of directions is increased, the weight of the band closest to the wall is decreased. This direction, as previously discussed, is the one experiencing the highest absorption. At the same time, the number of bands that are being treated by the same RTE integration distance increases with the number of transmission directions. Both of these effects will lead to a prediction of higher radiative intensity at the wall, relative to the tangent slab method. Once the method is modified to include a more accurate integration length, the results returned for a uniform radiating slab will be more accurate than a traditional $2\pi I$ approximation, and will more closely match the distribution from Equation 25.

5.2 FIRE-II

The FIRE-II vehicle was examined at the 1636 second point in its trajectory. This point was selected because it is in the data collection window for the first heat-shield, however it was late enough in the trajectory where a significant amount of radiation was measured. Relevant flight parameters for this point in the trajectory are presented in Table 4. The free stream chemical composition is given in terms of mass fractions in Table 5.

Table 4   Flight parameters for FIRE-II, 1636s

Parameter	Value
Wall Temperature	810 K
Free Stream Temp	215 K
Mach No.	38.5
Reynolds Number	47426
Free Stream Pressure	5.8 Pa

Table 5   Free stream mass fractions

Species	Fraction
N_2	.767
O_2	.233
N	1E-6
O	1E-6
NO	1E-6
NO^+	1E-6

The vehicle surface was modeled using a super-catalytic boundary condition. With a super-catalytic wall, free-stream species mass fractions are enforced at the wall. While it is known that the beryllium material used in the experiment was not catalytic to this extent, this boundary condition is consistent with the models used in other published works [8].

The spectral resolution used for the radiation calculation was driven by the need to compare radiative surface intensity with the FIRE-II experiment. As in the FIRE experiment, the lower bound of radiation wavelength was driven by the window cutoff in the VUV region [14], 2000 Angstrom ($0.2\mu m$). The upper wavelength bound was set at 15,000 Angstrom ($1.5\mu m$). A spectral resolution of 100,000 points was used. Sixteen transmissions were considered in the non-uniform radiation propagation method. A list

of radiation bands considered in this case are give in Table 6. The flow species were assumed to have attained an equilibrium population distribution of energy states, therefore SPRADIAN did not consider radiation due to non-equilibrium distributions. Bound-free transitions were not considered for atomic species because the NH7Air flow solver does not account for ionized oxygen or nitrogen.

Table 6   Radiation bands and mechanisms considered

Species	Mechanism
N_2	1^+
	2^+
	W
	BH1
	BH2
	WJ
	CY
O_2	SR
	cont
NO	γ
	β
	δ
	ϵ
N	bound-bound
	free-free
O	bound-bound
	free-free

5.2.1 Flowfield.   NH7Air was used to acquire a flow solution prior to conducting the radiation calculation. The flowfields used in this case were converged to three orders of magnitude. Accurate species concentrations and temperatures are necessary for SPRA-DIAN to determine the emission and absorption coefficients in each cell. The grid used for the FIRE-II case is shown in Figure 12. Shown in that figure is the initial grid and the final grid following several calls to the grid adaptation routine. Note that the two images in the figure use the same scale.

Figure 13 shows contours of heavy-particle translational temperature and concentrations of the N atom. It is clear from the figure that the flowfield around the FIRE-II
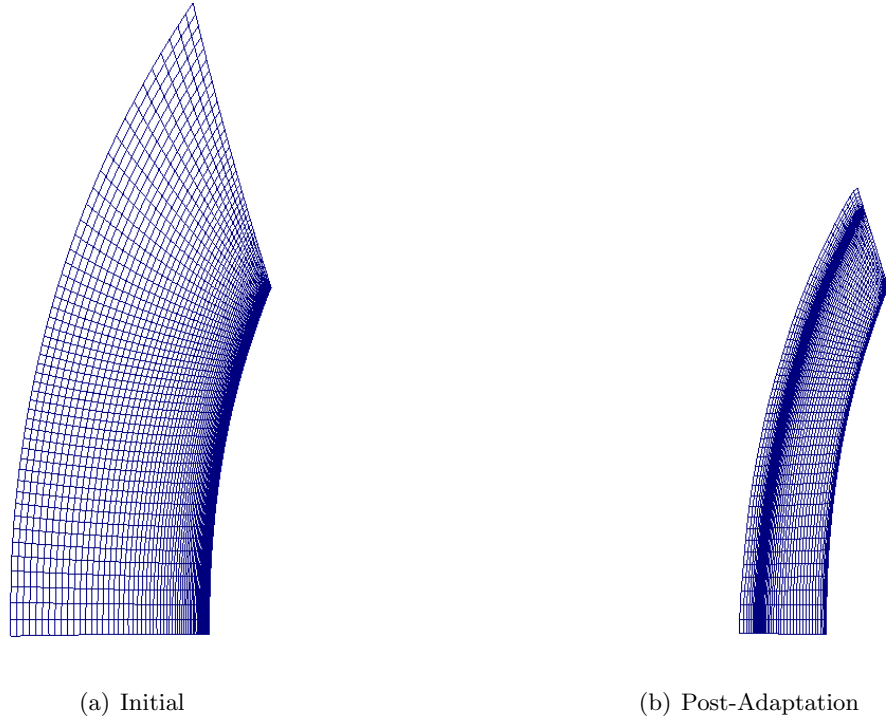
(a) Initial

(b) Post-Adaptation

Figure 12   FIRE-II grid

vehicle is relatively uniform, so reasonable agreement is expected between the new radiation propagation method and the tangent-slab method.

Stagnation line species concentrations are shown in Figure 14. In this figure, the primary free stream gases are represented by a solid line, atomic gases are represented by a dashed line, and trace gases are represented by a dotted line. As the gas passes the shock, it quickly dissociates into its constituent atoms. A thin region exists were NO forms, however it is quickly ionized into NO^+. Stagnation line temperatures are shown in Figure 15. Translational temperature peaks just behind the shock at 36,000K. After a short relaxation distance, the vibrational temperatures of the diatomic species equilibrate with the translational temperature at about 22,000K.

5.2.2   Radiation.   Contours of the coefficients of emissivity and absorptivity integrated over wavelength are presented in Figure 16. The shock layer radiates strongly in the region where the atomic species are present, with a maximum emission coefficient of 448
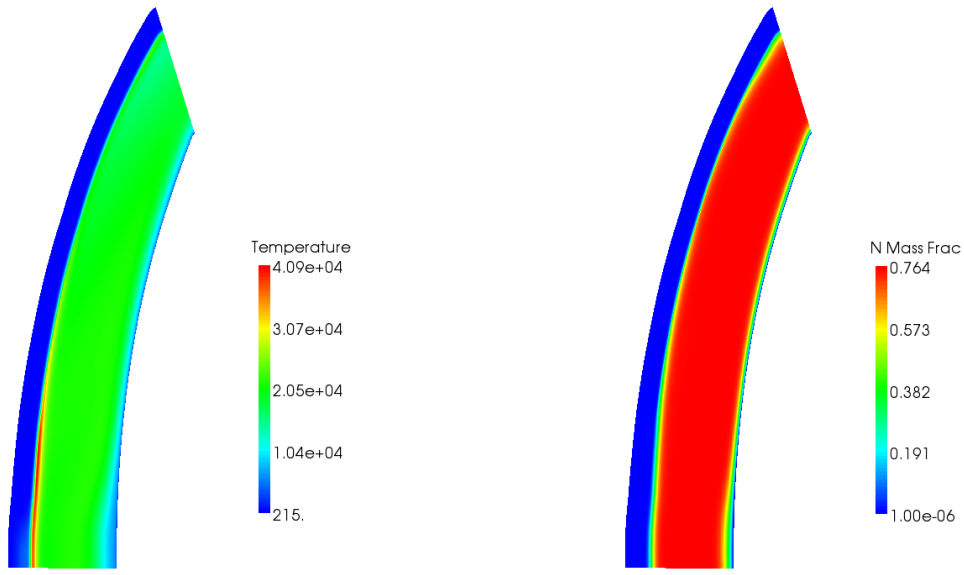
(a) Temperature

(b) N mass fraction

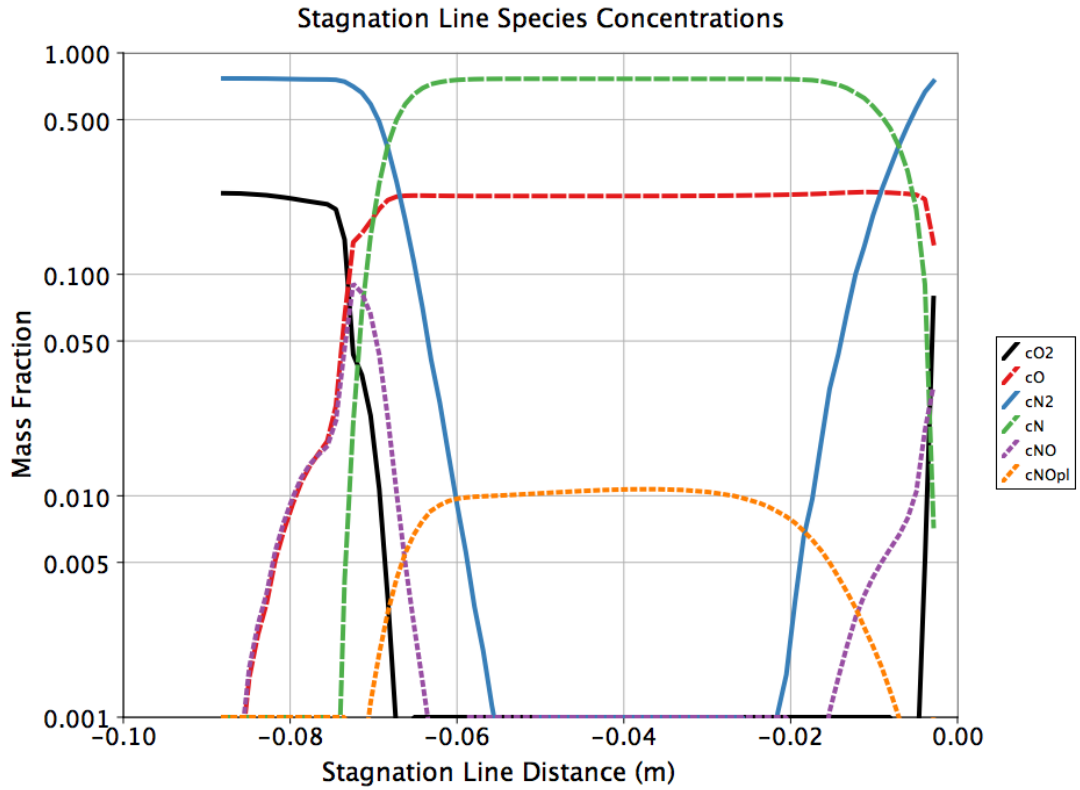Figure 13   Contours of temperature and nitrogen concentration in FIRE-II flowfield

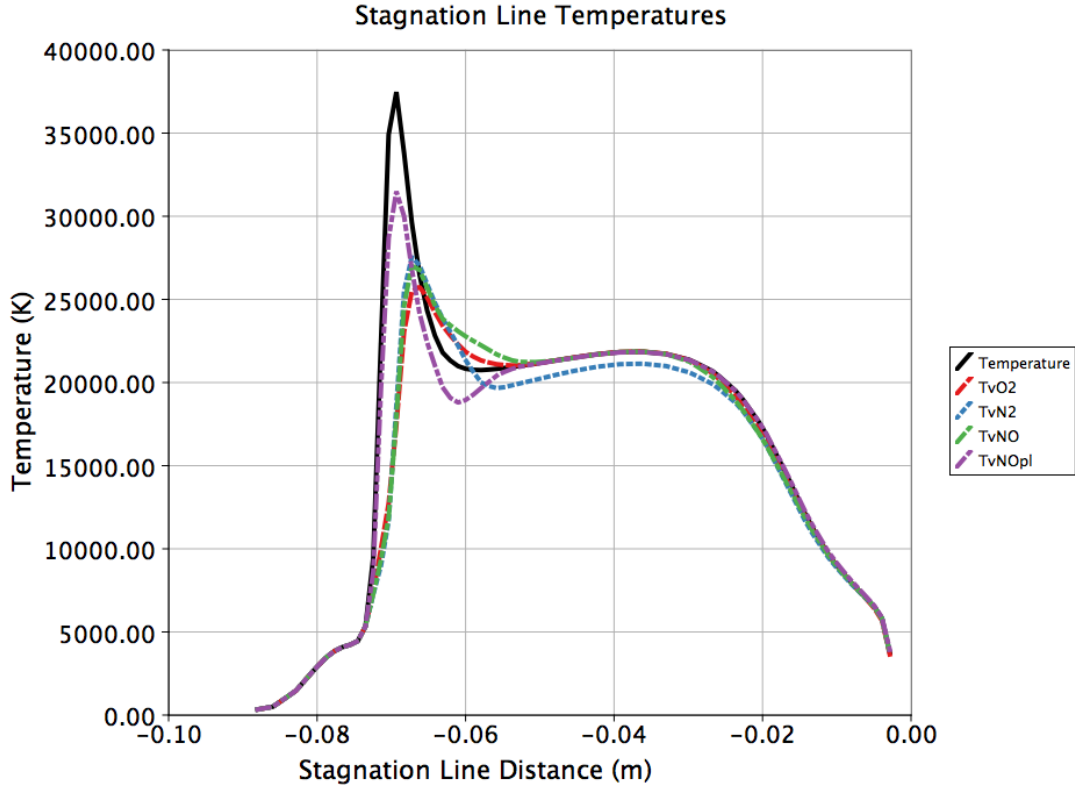Figure 14   Stagnation-line species concentrations for FIRE-II

41

Figure 15   Stagnation-line temperatures for FIRE-II

W/cm^2-st. The emission coefficient is low for the cold gas in the boundary layer, as would
be expected. Areas with high emission coefficients also have high absorption coefficients.
The absorption coefficient in the shock layer peaks at 0.035 cm^{-1}. While the absorption
coefficient itself is low in the boundary layer, the complete lack of emission in this region
make the net effect highly absorptive. Note that the areas of high absorption in the free
stream are spurious calculations that result from attempting to predict radiative proper-
ties in a cool, non-radiating free stream gas. Radiation solvers, such as SPRADIAN, are
designed to predict radiative properties in shock-layers only, and can give unpredictable
results in areas of low species concentrations at low temperatures. All points ahead of
the shock were not included in the non-uniform radiation propagation method, and hence
the cells with spurious absorption did not affect the overall radiation solution. Additional
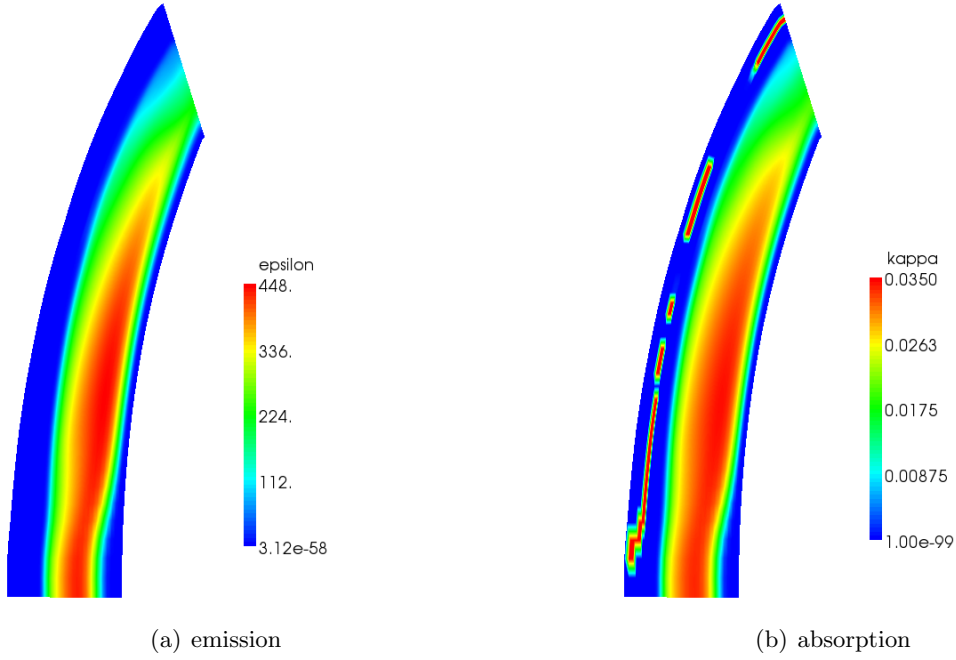contours of FIRE-II radiation properties are presented in Appendix A.

<div align="center">(a) emission   (b) absorption</div>

Figure 16   Emission $[W/cm^3 - st]$ and absorption $[1/cm]$ coefficient for FIRE-II 1636s

Predicted surface radiative flux is presented in Figure 17 as a function of y-ordinate on the vehicle surface. For this calculation, the normal intensity predicted by the tangent slab method was multiplied by a 2π hemispherical solid angle to return the radiative heat flux. The directional intensities predicted by the new method were integrated as piece-wise bands of a hemisphere to return the total radiative flux in that method.

Figure 17 shows the non-uniform method predicting a 9% lower radiative flux at the stagnation point when compared to the tangent slab method. As has been previously discussed, the tangent-slab method is expected to over-predict the flux in this scenario due to the assumption of strict uniformity in the flowfield. Agreement is poorer away from the stagnation point with the disagreement increasing to 60%, which is also not unexpected due to the lower degree of uniformity in this region of the flow.

Comparison to the values of radiative intensity measured in the FIRE-II experiment is given in Table 7. The radiometer in the FIRE-II experiment had a narrow ten-degree included angle field of view, so a comparison is presented of radiative intensity on the radiometer, not total radiative heat flux. The tangent slab wall normal intensity was used
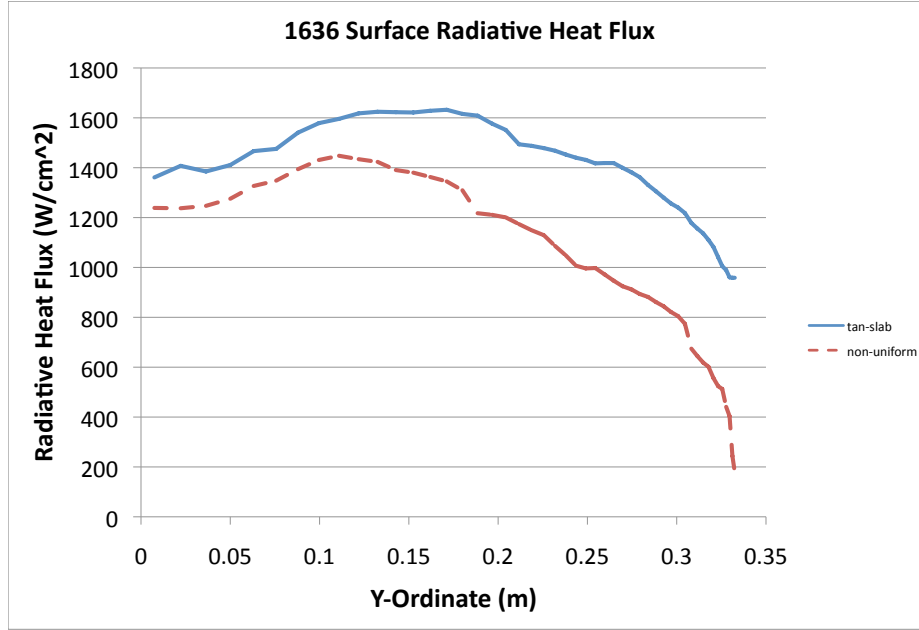
1636 Surface Radiative Heat Flux

Figure 17   FIRE-II 1636s total surface intensity

directly, while the non-uniform intensity was selected from the direction that best aligned with the wall normal. While both the tangent-slab method and non-uniform method very reasonably with one another, they both vary significantly from the value measured in the experiment.

Table 7   Radiative intensity on stagnation radiometer for FIRE-II, 1636s

Model	Intensity $[W/cm^2 - st]$
Experiment	4.5
Tangent Slab	98.8
Non-uniform	98.7

The fact that these two methods, which are built on different assumptions, share the same error when compared to experimental data leads one to believe that the error rests in an element common to both methods. Both methods used the same flowfield to conduct their respective radiation analysis, so the error may lie with the predicted

flowfield properties. As was previously mentioned, the flowfield had converged three orders of magnitude prior to the radiation routines being invoked. Because of the T^4 sensitivity of radiation, further convergence may lead to a more accurate radiation solution. Both methods also use the same SPRADIAN emission/absorption coefficient routines, and RTE integration routines. It is conceivable that the error lies within the SPRADIAN code, however the extent to which SPRADIAN has been validated by other researchers makes this an unlikely possibility.

6. CONCLUSIONS

A new method was developed to predict the radiative heat load on an arbitrary axisymmetric hypersonic vehicle. This method represents two major advances in atmospheric radiation prediction. First, the method considers the internal energies of each diatomic species separately, providing increased accuracy to the determination of the population of the excited states. Second, the method does not impose the assumption of a uniform flowfield, making it applicable slender re-entry bodies.

6.1   Method Effectiveness

The non-uniform radiation propagation algorithm was shown to correctly reproduce the radiative intensity on a surface due to a uniform radiating slab. It was shown that agreement with the tangent slab model improves for this case with an increasing number of transmission directions, however sixteen directions were sufficient to produce results with less than 5% error.

The method was successfully applied to the FIRE-II 1636s trajectory point, showing good agreement with the tangent slab model, however both models showed poor agreement with the experimental data. The agreement was accomplished without imposing the assumptions of a uniform radiation field. Therefore, this method may be applicable to slender bodies in hypersonic reentry, whereas the tangent slab model would not be applicable.

One limiter in the performance of the multi-temperature combined flow-field radiation model was the stiffness of the flow solver. For the FIRE-II case, the numerical stiffness imposed by the chemical source terms led to low CFL numbers and exceedingly slow convergence. Given that radiation properties are a function of T^4, a converged flow solution is requisite for an accurate radiation solution.

While this method was shown to be applicable for radiative flows, it is by no means computationally efficient, nor was it intended to be. The memory requirements required to store the radiative intensity information in each cell was a limiting factor for the cases examined in this study. Typical cases required between 30 gigabytes and 60 gigabytes of physical memory. Additionally, the non-uniform radiation calculations were orders of

magnitude more costly in terms of CPU time, when compared to the requirements of the tangent slab analysis. The new method is physically more accurate than the tangent slab method, at the cost of computational resources and efficiency.

6.2   Recommendations for Further Study

For problems of interest, it would be necessary to add additional chemistry to the flow solver used in this study. At a minimum, the chemistry set should be expanded to include a traditional 11-species air model ($N_2, O_2, N, N^+, O, O^+, NO, NO^+, N_2^+, O_2^+, e^-$). Additional chemistry would be need to to model the carbonic species introduced through ablation.

It may be worth considering developing an implicit treatment of the flowfield update in NH7Air. The current version of the code is time explicit, requiring exceedingly small CFL numbers to remain stable due to the strong influence of the chemical source terms. CFL numbers of between 10^{-6} and 10^{-2} were typically required for this study. The slow convergence led to exceedingly long run times.

In the radiation portion of the code, the effect of the choice of integration length should also be examined. Correct determination of the integration length may lead to more accurate absorption calculations in the near wall regions. Additionally, the radiative energy flux needs to be loosely coupled to the overall flow solution. A series of alternating flow solutions and radiation solutions should be run, each to convergence. Once each radiation solution has converged, the divergence of radiative heat flux should be applied as a static source term for the next series of flowfield updates.

Finally, some effort should be given to increasing the computational efficiency of the integrated flow-solver radiation package. In its current implementation, the combined solvers are loosely parallelized using the OpenMP architecture. A rigorous parallelization would decrease computational time, enabling a more efficient use of shared computing resources. Additional optimization could be performed to reduce the amount of physical memory required by the radiation calculation.

Appendix A. FIRE-II Contours

Figure 18(a) shows contours of wall normal radiative intensity. Figure 18(b) shows contours of $+x$ direction radiative intensity. The disagreement in the contours in the top of the domain are due to the following reasons. First, in the upper part of the domain the $+x$ direction does not align with the wall normal direction. Second, the zero gradient imposed on the radiation boundary in figure 18(b) is not an entirely accurate assumption in this case. Third, the radiation routines may have been invoked too early with respect to the global flowfield convergence.

Figure 19 shows the difference between the two predicted radiation fields. The units of the figure are $[W/cm^2 - st]$. The highest observed intensities using both methods was approximately 280 $[W/cm^2 - st]$. There is very good agreement in the stagnation region, with poorer agreement at the edge of the domain.

Figure 20 shows contours of radiative intensity away from the wall, and in the $-x$ direction respectively.

Figure 21 shows the difference between the predicted intensities in the $-x$ direction. Figure 21(a) shows the difference in the units of $[W/cm^2 - st]$, Figure 21(b) shows the difference as a percentage variation. Agreement is very good in the stagnation region, and poorer towards the edge of the domain.

Figure 22 shows contours of radiative intensity in directions tangental to the wall. This is information that is not taken into account by the tangent-slab method.
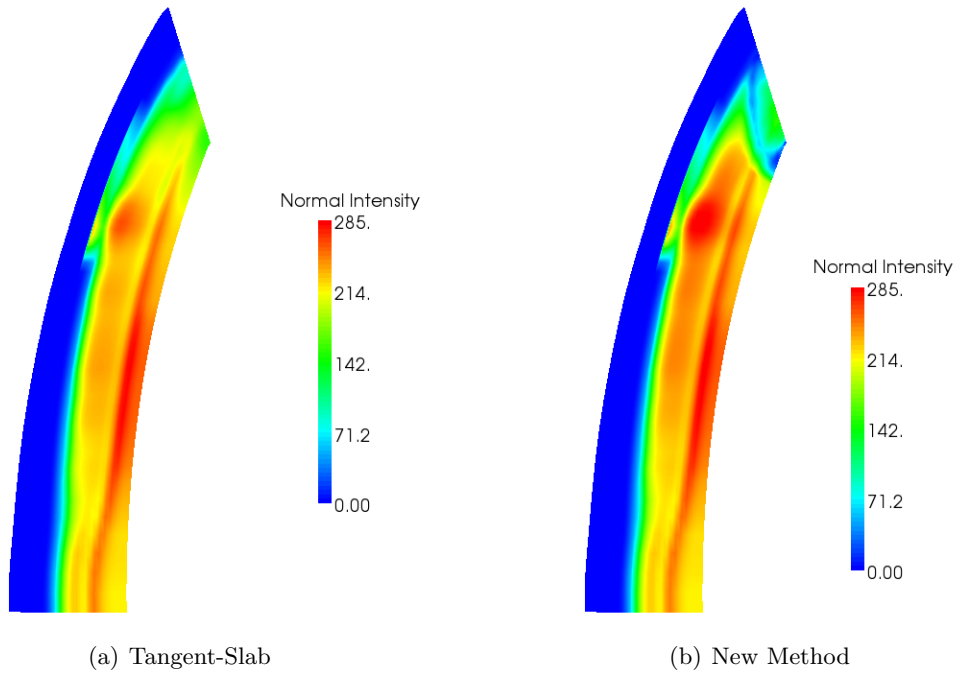
(a) Tangent-Slab

(b) New Method

Figure 18   Predicted intensity towards the wall in FIRE-II flowfield $(W/cm^2 - st)$
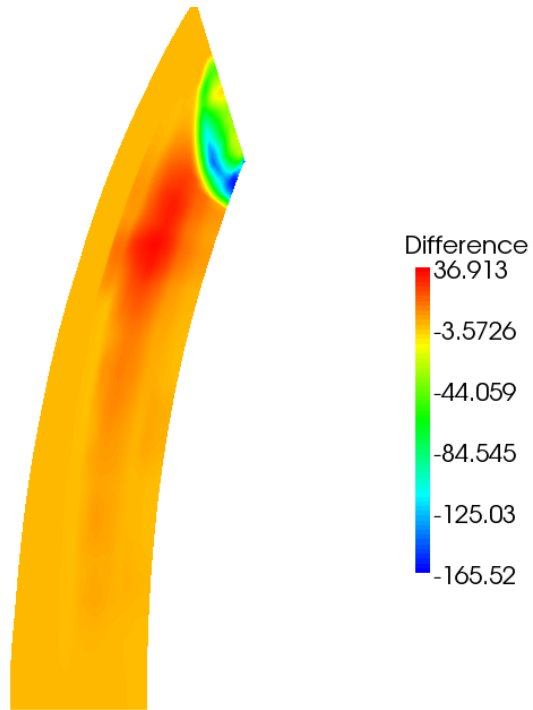
Figure 19   Difference in normal intensity $(+x)$

49

(a) Tangent-Slab

(b) New Method
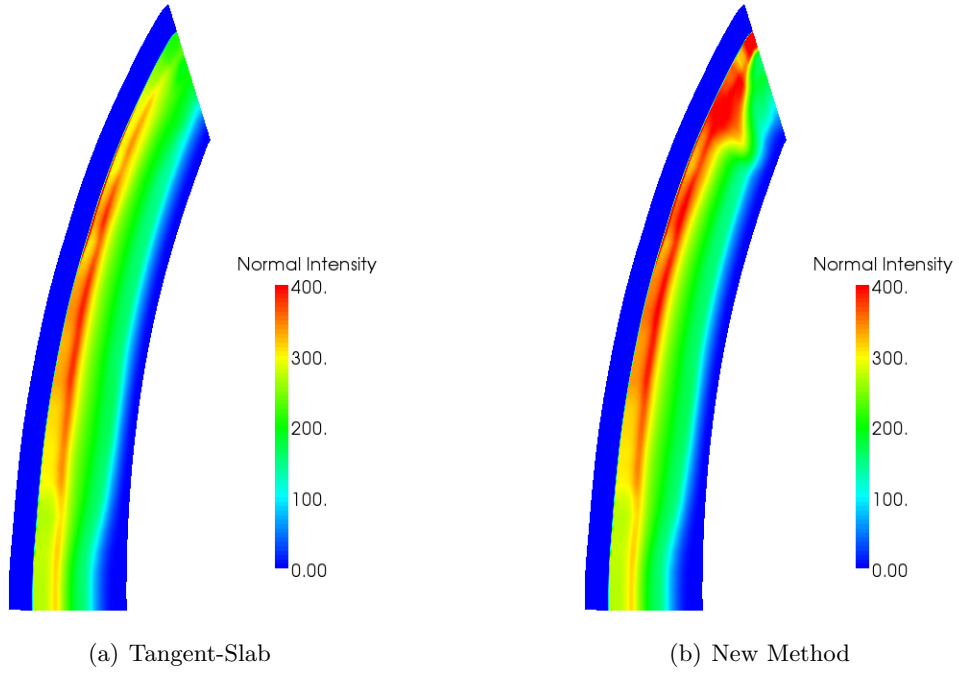
Figure 20   Predicted intensity away from the wall in FIRE-II flowfield $(W/cm^2 - st)$

(a) Difference

(b) % Difference
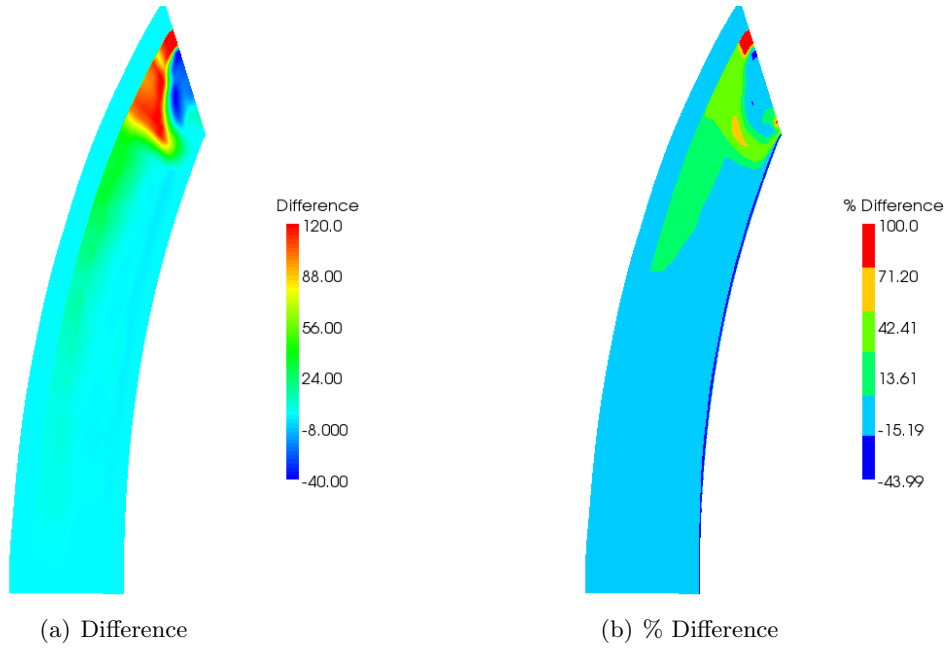
Figure 21   Difference in normal intensity $(-x)$

(a) $+y$ (b) $-y$
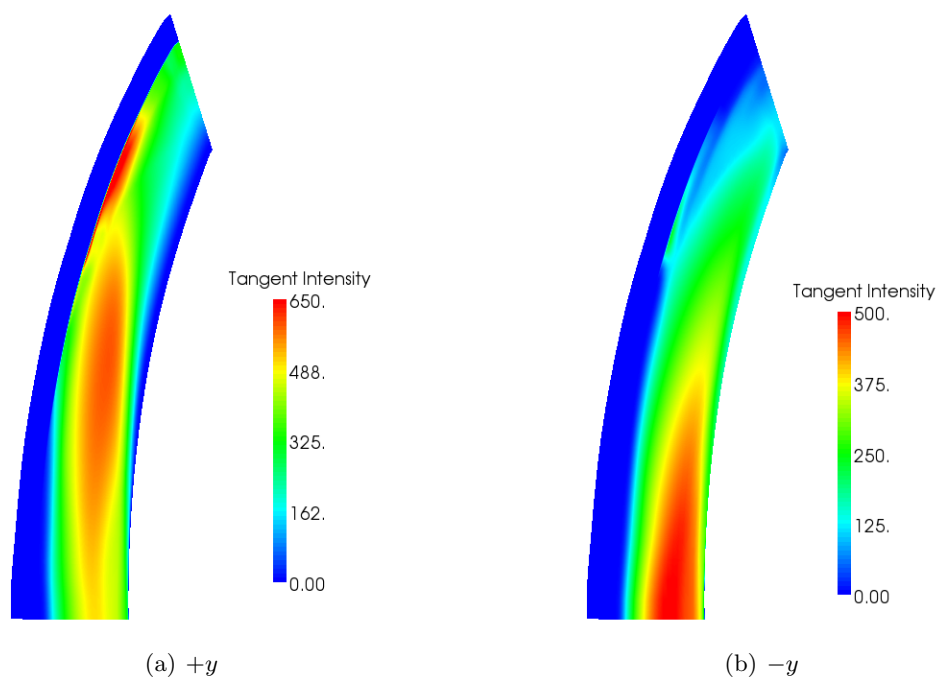
Figure 22   Predicted intensity tangential to the wall in FIRE-II flowfield $(W/cm^2 - st)$

Nomenclature

A	=	Heavy particle
A_{ul}	=	Einstein A coefficient for bound-bound emission
B_{lu}	=	Einstein B coefficient for induced absorption
B_{ul}	=	Einstein B coefficient for induced emission
C_f	=	Activation energy
D	=	Effective diffusion coefficient
E	=	Approximate electric field
F_{bl}	=	Boundary layer placement term
F_{sh}	=	Shock placement term
I	=	Radiation intensity
J	=	Rotational state
K	=	Effective optical depth
P	=	Pressure
Q	=	Energy exchange between modes
R_{bf}	=	Bound-free reduction factor due to spontaneous emission
T	=	Temperature
V	=	Effective diffusion velocity
Z	=	Ionic valency
Ω	=	Solid angle
Φ	=	Line broadening factor
α_{dir}	=	Overlap in radians between transmission direction and cell neighbor
β	=	Total included angle of transmission direction
$\dot{\omega}_s$	=	Species generation or destruction
ϵ	=	Elementary electronic charge
ϵ_0	=	Grid clustering term
η'	=	Thermal conductivity coefficient
κ	=	Coefficient of absorptivity $[1/s]$
μ	=	Molecular viscosity
σ_{ff}^{z-1}	=	Integrated electron velocity distribution

σ_{lu}	=	Bound-free cross section
τ^{ij}	=	Viscous shear stress
θ_d	=	Characteristic temperature of dissociation
ε	=	Coefficient of emissivity $[W/cm^3 - st - \mu m]$
a	=	Local speed of sound
c	=	Speed of light
c	=	View coefficient from cell to given neighbor in direction dir
e	=	Electron
e	=	Specific energy
g	=	Degeneracy ratio
h	=	Planck's constant
$h\nu$	=	Energy quanta, photon
k	=	Boltzmann's constant
k_f	=	Forward rate coefficient
m_e	=	Mass of an electron
n	=	Number density $[1/cm^3]$
q	=	Heat flux
q_r	=	Radiative flux
r, θ, ϕ	=	Cylindrical ordinates
u	=	Velocity
x	=	Position component

Subscripts

λ	=	Function of wavelength
i, j	=	Cell indices
l	=	Lower state
n	=	Neighboring cell
s	=	Species
u	=	Upper state
v	=	Vibration
eff	=	Effective

| bb | = | Black-body |
| ave | = | Average value |

Superscripts

| i,j | = | ith and jth components in orthogonal coordinates |
| z | = | Ionic Valence |

Bibliography

1. Michael J Wright, Deepak Bose, and Joseph Olejniczak, "Impact of Flowfield-Radiation Coupling on Aeroheating for Titan Aerocapture," *Journal of Thermophysics and Heat Transfer*, vol. 19, no. 1, pp. 17 – 27, January - March 2005.

2. L C Hartung, *Nonequilibrium Radiatie Heating Prediction Method for Aeroassist Flowfields with Coupling to Flowfield Solvers*, Ph.D. thesis, North Carolina State University, 1991.

3. F M Cheatwood and P A Gnoffo, "User's Manual for the Langley Aerotermodynamic Upwind Relaxation Algorithm (LAURA)," NASA TM 4674, National Air and Space Administration, April 1996.

4. Chul Park, *Nonequilibrium Hypersonic Aerothermodynamics*, John Wiley & Sons, New York, 1990.

5. Ian D Boyd, Jiaqiang Zhong, Deborah A Levin, and Peter Jenniskens, "Flow and Radiation Analyses for Stardust Entry at High Altitude," 2008-1215, 46th Aerospace Sciences Meeting and Exhibit, January 2008.

6. A M Feldick, M Modest, and D A Levin, "Closely Coupled Flowfield-Radiation Interactions For Flowfields Created During Hypersonic Reentry," 2008-4104, 40th AIAA Thermophysics Conference, June 2008.

7. Peter A Gnoffo, "Implementation of Radiation, Ablation, and Free Energy Minimization Modules for Coupled Simulations of Hypersonic Flow," 2009-1399, 47th AIAA Aerospace Sciences Meeting, January 2009.

8. David Hash, Joseph Olejniczak, Michael Wright, Dinesh Prabhu, Maria Pulsonetti, Brian Hollis, Peter Gnoffo, Michael Barnhardt, Ioannis Nompelis, and Graham Candler, "FIRE II Calculation for Hypersonic Nonequilibrium Aerothermodynamics Code Verification: DPLR, LAURA, and US3D," 2007-605, 45th AIAA Aerospace Sciences Meeting, Reno, Nevada, January 2007.

9. Christopher O Johnston, Peter A Gnoffo, and Kenneth Sutton, "The Influence of Ablation on Radiative Heating for Earth Entry," 2008-4107, 40th AIAA Thermophysics Conference, June 2008.

10. Christopher O Johnston, Brian R Hollis, and Kenneth Sutton, "Nonequilibrium Stagnation-Line Radiative Heating for Fire II," *Journal of Spacecraft and Rockets*, vol. 45, no. 6, pp. 1185 – 1195, November-December 2008.

11. Leonardo C Scalabrin and Ian D Boyd, "Numerical Simulations of the FIRE-II Convective and Radiative Heating Rates," 2007-4044, 39th AIAA Thermophysics Conference, June 2007.

12. C Park, "Nonequilibrium Air Radiation (NEQAIR) Program: Users Manual," NASA TM 86707, National Air and Space Administration, July 1985.

13. John H Lewis and William I Scallion, "Flight Parameters and Vehicle Performance for Project FIRE Flight II, Launched May 22, 1965," Nasa tn d-3569, National Air and Space Administration, 1966.

14. Dona L Cauchon, "Radiative Heating Results from the FIRE II Flight Experiment at a Reentry Velocity of 11.4 Kilometers per Second," NASA TM X-1402, National Air and Space Administration, April 1972.

15. Elden S Cornette, "Forebody Temperatures and Calorimeter Heating Rates Measured During Project FIRE II Reentry at 11.35 Kilometers per Second," NASA TM X-1305, National Air and Space Administration, 1966.

16. Robert B Greendyke and Lin C Hartung, "A Convective and Radiative Heat Transfer Analysis for the Fire II Forebody," 93-3194, 24th AIAA Plasmadynamics & Lasers Conference, July 1993.

17. David R Olynick, W D Henline, Lin Hartung, and G V Candler, "Comparisons of Coupled Radiative Navier-Stokes Flow Solutions with the Project Fire II Flight Data," 94-1955, 6th AIAA/ASME Joint Thermophysics and Heat Transfer Conference, June 1994.

18. Ya. B. Zel'dovich and Yu. P. Raizer, *Physics of Shock Waves and High-Temperature Hydrodynamic Phenomena*, Dover Publications, Mineola, NY, 1967.

19. Michael F Modest, *Radiative Heat Transfer*, McGraw - Hill, New York, 1993.

20. Kazuhisa Fujita and Takashi Abe, "SPRADIAN, Structured Package for Radiation Analysis: Theory and Application," Report 669, The Institute of Space and Astronautical Science, September 1997.

21. Eswar Josyula and William F Bailey, "Governing Equations for Weakly Ionized Plasma Flowfields of Aerospace Vehicles," *Journal of Spacecraft and Rockets*, vol. 40, no. 6, pp. 845–857, November-December 2003.

22. Peter A Gnoffo, Lin C Hartung, and Robert B Greendyke, "Heating Analysis for a Lunar Transfer Vehicle at Near-Equilibrium Flow Conditions," 93-0270, 31st AIAA Aerospace Sciences Meeting and Exhibit, Reno, Nevada, January 1993.

REPORT DOCUMENTATION PAGE

Form Approved
OMB No. 0704–0188

1. REPORT DATE (DD–MM–YYYY)	2. REPORT TYPE	3. DATES COVERED (From — To)
26-03-2009	Master's Thesis	1 Mar 08 - 26 Mar 09

4. TITLE AND SUBTITLE

Development of Non-Uniform Radiation Solution Methods for Atmospheric Re-entry Using Detailed Thermal Modeling

5a. CONTRACT NUMBER

5b. GRANT NUMBER

5c. PROGRAM ELEMENT NUMBER

6. AUTHOR(S)

Jeffrey R. Komives, Capt USAF

5d. PROJECT NUMBER

5e. TASK NUMBER

5f. WORK UNIT NUMBER

7. PERFORMING ORGANIZATION NAME(S) AND ADDRESS(ES)

Air Force Institute of Technology
Graduate School of Engineering and Management (AFIT/ENY)
2950 Hobson Way
WPAFB OH 45433-7765

8. PERFORMING ORGANIZATION REPORT NUMBER

AFIT/GAE/ENY/09-M13

9. SPONSORING / MONITORING AGENCY NAME(S) AND ADDRESS(ES)

Dr. John Schmisseur, Air Force Office of Scientific Research
875 N Randolph St, Arlington VA, 22203
john.schmisseur@afosr.af.mil
DSN: 426-6962

10. SPONSOR/MONITOR'S ACRONYM(S)

AFOSR

11. SPONSOR/MONITOR'S REPORT NUMBER(S)

12. DISTRIBUTION / AVAILABILITY STATEMENT

APPROVED FOR PUBLIC RELEASE; DISTRIBUTION UNLIMITED

13. SUPPLEMENTARY NOTES

14. ABSTRACT

The line-by-line accurate spectral radiation solver SPRADIAN was integrated with the multi-temperature hypersonic flow-solver NH7Air for the purpose of predicting the radiation incident on the surface of a hypersonic re-entry vehicle. Atomic and molecular radiation mechanisms are considered for chemical species present in an Earth atmosphere re-entry. A new numerical method of radiation propagation is presented that is capable of accurately predicting the radiation propagation through a non-uniform radiation field. This method also introduces a unique treatment of the internal energy of each chemical species, independently tracking the vibrational temperatures of all molecular species.

The new radiation propagation method is validated against the industry standard tangent-slab method for a uniform radiating slab. Results are also presented for the 1636 second trajectory point of the NASA FIRE-II experiment. For the FIRE-II case, the results of the new method is compared to the results of the tangent-slab analysis, and with the values measured in the experiment.

15. SUBJECT TERMS

Hypersonics, Radiation, Re-entry, CFD

16. SECURITY CLASSIFICATION OF:			17. LIMITATION OF ABSTRACT	18. NUMBER OF PAGES	19a. NAME OF RESPONSIBLE PERSON
a. REPORT	b. ABSTRACT	c. THIS PAGE	UU	68	Dr Robert Greendyke, Associate Professor
U	U	U			19b. TELEPHONE NUMBER (Include Area Code) (937) 255-3636x4567 robert.greendyke@afit.edu

Standard Form 298 (Rev. 8–98)
Prescribed by ANSI Std. Z39.18